

# **$\beta$ III spectrin is required for orthogonal wiring between Purkinje cell dendrites and granule cell axons in the murine cerebellar circuit**

**Kazuto Fujishima<sup>1\*</sup>, Junko Kurisu<sup>1</sup>, Midori Yamada<sup>1,2</sup>, Mineko Kengaku<sup>1,2</sup>**

1. Institute for Integrated Cell-Material Sciences (KUIAS-iCeMS), Kyoto University, Kyoto, 606-8501, Japan
2. Graduate School of Biostudies, Kyoto University, Kyoto, 606-8501, Japan

\* corresponding author: [fujishima@icems.kyoto-u.ac.jp](mailto:fujishima@icems.kyoto-u.ac.jp)

**Keywords:**  $\beta$ III spectrin,  $\alpha$ II spectrin, membrane skeleton, dendrite development, dendrite morphology, dendrite guidance, Purkinje cell, parallel fiber, SCA5, nanofiber

# Abstract

The wiring pattern of the neural circuit determines its function and properties. However, the mechanisms underlying the influence of the geometrical patterns of axonal and dendritic arbors on each other remain elusive. The cerebellar circuit displays an orthogonal topology in which Purkinje cell dendrites lie in a single parasagittal plane and form perpendicular contacts with the afferent granule cell axons running along the mediolateral axis. We utilize electrospun nanofibers to align granule cell axons and reproduce perpendicular contacts between Purkinje cell dendrites and granule cell axons in flat culture dishes. We show that the dendritic protein  $\beta$ III spectrin, a causal gene for spinocerebellar ataxia type 5 (SCA5), is required for the dendritic arborization geometry guided by afferent axonal bundles.  $\beta$ III spectrin deficiency interferes with the biased growth of dendrites perpendicular to axonal arrays on aligned nanofibers.  $\beta$ III spectrin deficiency causes the mislocalization of actin and excessive microtubule invasion in dendritic protrusions, resulting in ectopic branch formation in abnormal orientations. We also show that disease-associated mutations affect the ability of  $\beta$ III spectrin to control dendrite orientation. We provide evidence that  $\beta$ III spectrin organizes dendritic cytoskeletal structures required to steer the oriented growth of dendrites within neural circuits.

## Introduction

Neural circuits are constructed via the connection of axons and dendrites in characteristic geometric patterns. The neuronal wiring patterns are organized by various guidance mechanisms during development. Growing neurites often navigated according to the gradient of chemical environmental cues, including soluble and substrate-bound molecules. Neurites are also guided by physical contact with surrounding neurons. For instance, the growing dendrites of some neuron types, including cerebellar Purkinje cells, retinal amacrine cells and *Drosophila* DA neurons, undergo contact-based repulsion, which ensures the tiling and/or nonoverlapping arrangement of the dendrites of a given group of neurons (Fujishima et al., 2018; Grueber and Sagasti, 2010; Lefebvre, 2017). In contrast, axons often fasciculate with other axons of the same type and extend together to their target region (Cioni et al., 2018; Hayashi et al., 2014). In addition to axon-axon and dendrodendritic communications, the physical interaction between axons and dendrites has a great impact on the spatial organization of neural networks. However, the mechanisms determining how the spatial arrangement of axonal fibers affects the growth pattern of dendrites, or vice versa, are poorly understood (Chen et al., 2019; Ramirez-Suarez et al., 2019).

In the cerebellar cortex, the axons of cerebellar granule cells (GCs), also known as parallel fibers, run along the long axis of the cerebellum, while their synaptic target Purkinje cell (PC) dendrites elaborate their arbors in a single plane perpendicular to the parallel fibers (Figs. 2A and B). The orthogonal pattern seemingly contributes to the maximization of possible synaptic connections so that each PC dendrite contacts more than 100,000 parallel fibers (Napper and Harvey, 1988). Several lines of evidence suggest that the growth of PC dendrites in a direction perpendicular to the parallel fibers is involved in the arborization of unique flat dendrites (Nagata et al., 2006). However, the mechanisms regulating biased dendrite growth are largely unknown.

Spectrins are structural molecules that form a tetrameric complex with two alpha and two beta subunits. Spectrin tetramers interact with actin filaments beneath the plasma membrane. Recent studies using super-resolution microscopy have revealed that spectrin, actin, and their associated proteins form membrane periodic skeletal (MPS) structures lining the circumference of the axons and dendrites (D'Este et al., 2015; Han et al., 2017; Vassilopoulos et al., 2019; Xu et al., 2013). In the MPS, ring-like structures of actin are connected by spectrin tetramers with a periodicity of ~190 nm (quasi-1D structure). Alternatively, spectrin and associated proteins can form a 2D polygonal lattice structure in the soma or dendrites, possibly reminiscent of those found in erythrocytes (Han et al., 2017). These structures are considered to have multiple functions, such as the maintenance of membrane stiffness and/or elasticity (Krieg et al., 2017) and acting as a diffusion barrier to membrane molecules (Albrecht et al., 2016).

$\beta$ III spectrin, one of the beta subunits of spectrin molecules, is highly expressed in the

PC dendrites and soma.  $\beta$ III spectrin has been identified as a gene responsible for spinocerebellar ataxia type 5 (SCA5), which manifests as progressive dysfunction of motor coordination (Ikeda et al., 2006). PCs in SCA5 patients and  $\beta$ III spectrin knockout animals display aberrant dendrite morphologies due to abnormal arbor development and maintenance (Gao et al., 2011; Ikeda et al., 2006). Notably, the PCs of the  $\beta$ III spectrin knockout mouse exhibit a defect in flat dendrite arborization (Gao et al., 2011), implicating  $\beta$ III spectrin in the regulation of dendrite growth orientation.  $\beta$ III spectrin controls the localization and/or dynamics of transmembrane proteins such as the excitatory amino acid transporter (EAAT4), glutamine receptor GluR $\delta$ 2 (GluD2) and metabolic glutamate receptor 1 (mGluR1). The loss of  $\beta$ III spectrin thus leads to the mislocalization of these neurotransmitter receptors and transporters, which may cause progressive neurodegeneration via excitotoxicity (Armbrust et al., 2014; Perkins et al., 2010; Stankewich et al., 2010). However, the mechanisms by which  $\beta$ III spectrin controls dendrite development remain elusive.

Here, we show that  $\beta$ III spectrin is indispensable for the directed growth of PC dendrites perpendicular to parallel fibers, which leads to flat dendrite formation. We recapitulated a two-dimensional model of the orthogonal interaction between the dendrite and axonal bundles by using nanofibers as artificial scaffolds to control the orientation of parallel fiber arrays *in vitro*. We demonstrated that  $\beta$ III spectrin-deficient dendrites failed to form dendrites perpendicular to axonal bundles. Super-resolution observations confirmed the formation of repeated lattice-like structures of  $\beta$ III spectrin in PC dendrites.  $\beta$ III spectrin caused abnormal cytoskeletal dynamics and misoriented growth of dendrites. Our data provide insights into the role of  $\beta$ III spectrin in controlling the perpendicular connectivity of dendrites and axons.

## Results

### **$\beta$ III spectrin is required for a cell-autonomous mechanism of planar dendrite arborization in PCs**

We first confirmed the cell-autonomous role of  $\beta$ III spectrin in PC dendrite formation by short hairpin RNA (shRNA) knockdown *in vivo*. We used a plasmid encoding an shRNA targeting  $\beta$ III spectrin ( $\beta$ III spectrin kd) that efficiently knocks down  $\beta$ III spectrin expression in PCs in dissociation culture (Fig. S1). We sparsely delivered the plasmid into PC precursors in the 4th ventricle via *in utero* electroporation at embryonic day 11.5 (E11.5). Consistent with previous observations made using  $\beta$ III spectrin knockout mice, we observed almost no differences in the total length of dendrites between control (ctr) and  $\beta$ III spectrin kd cells at the developmental stage of postnatal day 14 (P14) (Figs. 1A-C). Compared to the normal planar dendrites in ctr PCs,  $\beta$ III spectrin kd cells exhibited misoriented dendrites that extended away from the main dendritic plane (Figs. 1A, B), similar to those in knockout animals (Gao et al., 2011). Indeed, quantitative analysis revealed that dendritic branches extruded from the main plane were significantly increased in  $\beta$ III spectrin kd PCs (Figs. 1A, B, and D and S2, see Materials and Methods), suggesting that a cell-autonomous function of  $\beta$ III spectrin is necessary for the planar dendrite formation of PCs.

### **Recapitulation of 2D perpendicular contact between PC dendrites and GC axons using artificial nanofibers *in vitro*.**

Next, we examined the mechanism underlying the effect the loss of  $\beta$ III spectrin on dendrite planarity. Considering the arrangement of flat PC dendrites closely aligned with neighboring PCs in the molecular layer (Fig. 2A), it seems unlikely that gradients of guidance molecules could guide such a dendritic configuration. It has previously been suggested that PC dendrites have the ability to grow perpendicularly to GC axons (Nagata et al., 2006). If dendrites grow perpendicularly to the bundle of parallel fiber axons that run along the coronal axis of the cerebellum, then dendrites will extend in parasagittal planes (Fig. 2B, left). We thus speculated that  $\beta$ III spectrin might be involved in dendrite growth perpendicular to GC axons.

To test this hypothesis, we first confirmed whether normal PC dendrites preferentially grow perpendicularly to GC axons. We established a simplified model in which parallel GC axons are recapitulated in 2D spaces (Fig. 2B, right). In this model, we utilized electrospun polycaprolactone nanofiber scaffolds, which have been used to navigate axonal extension in culture (Hyysalo et al., 2017). We plated dissociated cerebellar cells from P0 mice on aligned or randomly oriented nanofiber scaffolds. As expected, GC axons labeled with GFP (magenta) ran parallel to each other on aligned nanofibers (arrowheads in Fig. 2C), while they extended randomly on random nanofibers (arrowheads in Fig. 2E).

We previously reported that PCs in dissociated cerebellar cell culture initiate dendrites at approximately 8 days *in vitro* (8 DIV) and radially extend branches until at least 14 DIV (Fujishima et al., 2012). Likewise, the PC dendrites on the randomly oriented nanofibers were observed to grow radially with no directional preference (Fig. 2F). In contrast, the distribution of PC dendrites on the aligned nanofibers was highly biased toward the direction perpendicular to fibers, supporting the notion that PC dendrites grow perpendicularly to GC axons (Fig. 2D). The perpendicular growth was specific to PC dendrites, as PC axons grew parallel to GC axons (Fig. 2D). Furthermore, GC dendrites that were physically separated and did not form synaptic contacts with parallel fibers *in vivo* also grew in a random orientation on aligned fibers (Fig. 2C). These results suggest that the perpendicular interaction is not ubiquitous but rather specific to certain synaptic partners, including PC dendrites and GC axons.

It has been widely accepted that neuronal activities during network formation are involved in the selection of growing dendritic arbors. Thus, we assessed whether neuronal activity is required for the perpendicular growth of dendrites on aligned GC axons. However, the suppression of GC-PC synaptic activity by treatment with the AMPA/kinate receptor antagonist DNQX and the mGluR1 antagonist CPGCOEt had little or no effect on the perpendicular orientation of dendrites (Fig. S3).

### **Knockdown of $\beta$ III spectrin interferes with perpendicular contact.**

To confirm whether  $\beta$ III spectrin is required for perpendicular contact between PC dendrites and GC axons, we introduced shRNA plasmids to PCs and plated them on nanofiber substrates. In contrast to the dendrites perpendicular to nanofibers observed in ctr cells, a significant proportion of the dendritic branches in  $\beta$ III spectrin kd cells extended in different orientations (Fig. 3A). Quantitative morphometry revealed that the total length and number of dendritic branches were also increased in  $\beta$ III spectrin kd cells (Figs. 3B and C). Coexpression of shRNA-resistant  $\beta$ III spectrin reversed the changes in dendrite orientation, total length and branch numbers, negating the off-target effects of the knockdown construct (Figs. 3A-C,  $\beta$ III kd + rescue). Furthermore, the CRISPR/Cas9-based  $\beta$ III spectrin knockout PCs exhibited similar phenotypes on aligned nanofibers (Fig. S4). These results indicate that  $\beta$ III spectrin is required for perpendicular contact between PC dendrites and GC axons.

Spectrin molecules form tetrameric complexes composed of  $\alpha$  and  $\beta$  subunits, and the loss of  $\alpha$  subunits destabilizes  $\beta$  subunits in embryonic tissue (Stankewich et al., 2011). Among  $\alpha$ -spectrin subtypes,  $\alpha$ II spectrin is most abundant in non-erythrocytic cells (Cianci et al., 1999; Winkelmann and Forget, 1993). Indeed,  $\alpha$ II spectrin was strongly expressed in the PC somata and dendrites, similar to  $\beta$ III spectrin (Fig. 3D). We found that the knockdown of either  $\alpha$ II or  $\beta$ III spectrin dramatically reduced the levels of both proteins in PCs, suggesting the interdependency

of  $\alpha$ II and  $\beta$ III in the stabilization of the spectrin protein complex (Fig. 3D). Accordingly,  $\alpha$ II spectrin knockdown disrupted planar dendrite arborization *in vivo* (Fig. 3E) as well as biased dendrite organization on aligned nanofiber substrates (Fig. 3F). Taken together, these results indicate that the  $\alpha$ II/ $\beta$ III spectrin complex plays an important role in the regulation of dendrite orientation in PCs.

### Dynamic behavior of PC dendrites in nanofiber culture.

We have previously demonstrated that the nonoverlapping arrangement of PC dendrites is achieved by the contact-dependent retraction of growing branches (Fujishima et al., 2012). Thus, the perpendicular dendrites on nanofibers might be attributed to either (1) biased outgrowth in the perpendicular direction or (2) the biased retraction of misoriented branches. To distinguish between these possibilities, we performed time-lapse observations of growing dendrites on aligned nanofiber substrates. We followed the relatively slow outgrowth of PC dendrites ( $\sim 0.7$   $\mu$ m/hour) every three hours for several days from 8 DIV, when dendrite formation was initiated in the cultures (Fujishima et al., 2012). Ctr PCs continuously extended dendrites perpendicular to the fiber orientation (Figs. 4A and B, ctr). In addition, we observed only a few dendritic retractions. We therefore concluded that the perpendicular dendrite orientation in ctr PCs was likely due to biased dendritic growth, rather than the elimination of disoriented branches.

$\beta$ III spectrin kd cells also exhibited stable dendrite growth without massive dendritic retraction (Fig. 4A,  $\beta$ III kd). Although dendritic terminals growing in the perpendicular direction were still dominant in  $\beta$ III spectrin kd cells, the fraction of parallel-growing dendritic terminals was markedly increased to a level comparable to that of perpendicular terminals (Fig. 4B,  $\beta$ III kd).

Our previous studies have shown that PCs form dendritic branches primarily via the bifurcation of growing terminals (terminal branching), while they rarely extend collaterals from the shaft (lateral branching) (Fujishima et al., 2012). Accordingly, ctr PC dendrites on aligned fibers mainly display terminal branching (Fig. 4C and G). In contrast, lateral branching was found to be increased by more than 10-fold in  $\beta$ III spectrin kd dendrites compared with ctr dendrites (ctr,  $0.9 \pm 0.36\%$ ,  $n = 8$  cells vs  $\beta$ III  $10.0 \pm 1.8\%$ ,  $n = 8$  cells mean  $\pm$  SEM,  $p < 1.5 \times 10^{-4}$ ) (Fig. 4G), although the branching frequency was only slightly altered (Fig. 4H). The deflection angle between the bifurcated terminal branches ranged within approximately  $\pm 30^\circ$ , while that of lateral branching was greater than  $60^\circ$  in both the ctr and  $\beta$ III spectrin kd dendrites (Figs. 4E and F). The frequent lateral branching of the  $\beta$ III spectrin kd dendrites may contribute to the increase in misoriented dendrites. Furthermore, we observed that the bifurcated branch terminals often returned to a perpendicular orientation during 9 hours of observation in ctr cells (Fig. 4C arrow 40 hr and 50 hr, Fig. 4I). In contrast, most  $\beta$ III spectrin kd dendritic terminals never returned to a

perpendicular orientation with respect to nanofibers (Fig. 4D, arrows, Fig. 4I), suggesting that  $\beta$ III spectrin is required for the correction of misoriented branches. Taken together, these results suggest that  $\beta$ III spectrin regulates the perpendicular growth of dendrites by inhibiting lateral branching and steering the misoriented growth of dendrites.

### **Lateral branch formation in $\beta$ III spectrin-knockdown dendrites.**

We next observed how dendritic planarity was affected in  $\beta$ III spectrin kd cells in *in vivo* cerebellar tissue. Ctr PC dendrites transfected with GFP aligned in a parasagittal plane in the molecular layer parallel to the neighboring PC dendrites (Figs. 5A and B, ctr). These PCs rarely exhibited dendritic branches growing in lateral (coronal) directions. Neighboring dendrites were separated by gaps of approximately 1-3  $\mu$ m, showing minimal crossing with adjacent branches. Similar to ctr PCs, the main dendritic arbors of  $\beta$ III spectrin kd PCs were mostly parallel to neighboring PC dendrites in coronal sections (Figs. 5A and B,  $\beta$ III kd), although some dendrites bent or tilted into an incorrect planes (white arrows in Fig. 5A). Notably,  $\beta$ III spectrin kd dendrites exhibited an increased number of laterally oriented branches that grew into the territories of the neighboring PC dendrites (yellow arrows in Figs. 5A and C). These misoriented branches often turned and extended parasagittally into the gaps between PC dendrites (yellow arrowhead in Fig. 5A). These misoriented lateral branches likely contributed to the disruption of planar dendrite formation in  $\beta$ III spectrin kd PCs.

It has been demonstrated that the dendrites of growing PCs are covered with numerous dendritic protrusions, including dendritic filopodia and immature spines (Kawabata Galbraith et al., 2018; Shimada et al., 1998). As dendritic protrusions are known to serve as dendritic branch precursors in some neurons, we next analyzed the dendritic protrusions in PCs with or without  $\beta$ III spectrin expression. Ctr dendrites presented numerous dendritic protrusions emanating from the shaft with a mean length of  $1.48 \pm 0.04$   $\mu$ m (mean  $\pm$  SEM,  $n = 231$ ) (Figs. 5D and E). In contrast,  $\beta$ III spectrin kd dendrites exhibited significantly longer protrusions ( $2.21 \pm 0.17$   $\mu$ m,  $n = 102$ ,  $p < 10^{-7}$ , Student's t-test) (Figs. 5D and E) at a lower density (Fig. 5F), in agreement with previous studies (Efimova et al., 2017; Gao et al., 2011). Notably, some dendritic protrusions in  $\beta$ III spectrin kd cells were abnormally elongated ( $>5$   $\mu$ m) in lateral directions away from the main sagittal plane of the dendritic shaft (arrows in Fig. 5D, Fig. 5G). These long lateral protrusions seemed to serve as precursors of the ectopic lateral branches in  $\beta$ III spectrin kd cells.

### **Abnormal formation of dendritic protrusions in $\beta$ III spectrin-knockdown dendrites**

To further analyze the implications of  $\beta$ III spectrin in the formation of dendritic protrusions and branches, we observed the dendritic structures in neurons grown on aligned nanofiber substrates. Ctr PCs bore highly dense protrusions that covered the lateral surface of the dendritic shaft,

similar to those observed *in vivo* (Fig. 6A). These protrusions expressed glutamate receptor  $\delta 2$  (GluD2), which functions as a synaptic glue by binding with presynaptic neurexin and cbln1 in GC axonal terminals (Fig. 6A)(Matsuda et al., 2010; Uemura et al., 2010). The GluD2 signals were often weaker in the newly formed protrusions at the distal end of the growing dendrites, suggesting that the distal protrusions might not yet have bound to synaptic partners (Fig. 6A, F).

Compared to ctr cells, the distal dendrites of  $\beta$ III spectrin kd cells were significantly thinner (ctr:  $1.80 \pm 0.15 \mu\text{m}$ ,  $n = 19$  dendrites,  $\beta$ III kd:  $0.90 \pm 0.06 \mu\text{m}$ ,  $n = 22$  dendrites, mean  $\pm$  SEM,  $p = 7 \times 10^{-6}$ , Student's t-test) (Fig. 6B). In contrast to the dendritic protrusions in ctr cells, which presented a relatively constant length of 1-3  $\mu\text{m}$ , those in  $\beta$ III spectrin kd cells presented various lengths at a lower density, with an average length that was significantly longer than that in ctr cells (Figs. 6C and D). We found some abnormally elongated protrusions of nearly 10  $\mu\text{m}$  in  $\beta$ III spectrin kd dendrites that extended parallel to the orientation of nanofibers. Other short protrusions often appeared wider at their bases, reminiscent of the shaft synapses with deficient neck formation observed in  $\beta$ III spectrin kd hippocampal neurons (Fig. 6B ROI1)(Efimova et al., 2017). The extremely long protrusions exhibited multiple GluD2 puncta that were irregularly arranged along their lengths. These GluD2 signals sometimes clustered in dilations, implying contact sites with GC axons (Fig. 6B ROI2). The orientation of the protrusions in the ctr and  $\beta$ III spectrin kd dendrites was mostly parallel to that of the nanofibers, suggesting that they were associated with GC axons (Figs. 6E and 6F).

We next analyzed the subcellular localization of  $\beta$ III spectrin in growing dendrites in PCs cultured on coverslips. In agreement with previous reports (Efimova et al., 2017; Gao et al., 2011),  $\beta$ III spectrin was strongly localized on the surface of the dendritic shaft (Fig. 6G).  $\beta$ III spectrin spread into the base of dendritic protrusions but was excluded from their tips (Fig. 6H). Actin showed an inverse gradient along the dendritic protrusions, as revealed by HA-actin, such that it was densely localized at the tip and sharply declined in the base of the protrusion and the dendritic shaft (Figs. 6H and I). In contrast, actin was more widely distributed along the entire length of both long and thin (Type 1 in Fig. 6J) and short and stubby (Type 2 in Fig. 6J) dendritic protrusions and was often dispersed in the shaft of distal dendrites in  $\beta$ III spectrin kd PCs (Fig. 6J Type 1, K). These results imply that  $\beta$ III spectrin might be involved in the formation of the structural boundary between the dendritic shaft and protrusions that confines actin filaments within dendritic protrusions.

### Membrane periodic skeleton structure formed by $\beta$ III spectrin

Super-resolution microscopy has revealed that the spectrin/actin complex forms MPS structures, which might function as a diffusion barrier for membrane proteins (Albrecht et al., 2016; Leite et al., 2016). Using stimulated emission depletion microscopy (STED), we confirmed the existence

of MPS-like repeated structures composed of  $\beta$ III spectrin in the shaft regions of developing PC dendrites (Figs. S5A, S5C ROI1). The average interval of the repeated structures was  $186 \pm 5 \mu\text{m}$  (mean  $\pm$  SEM,  $n = 85$  peaks, Fig. S5D), consistent with previous studies (Xu et al., 2013). Actin rings were not clearly observed in the repeated structures, probably due to very low actin signals in the dendritic shafts of PCs (data not shown and Fig. 6H). Repeated  $\beta$ III spectrin structures were also observed along the narrow corridor of the neck region of dendritic protrusions (Figs. S5B and S5C: ROI2 and 3) with an interval of  $187 \pm 5 \mu\text{m}$  (mean  $\pm$  SEM,  $n = 93$  peaks, Fig. S5D). As previously demonstrated, the repeated spectrin structures were not continuous and were often interrupted by irregularly arranged signals, probably due to the lower propensity for repeated structure formation in dendrites (Fig. S5E and F)(D'Este et al., 2015; Han et al., 2017).

### **$\beta$ III spectrin suppresses microtubule entry into dendritic protrusions**

We demonstrated that  $\beta$ III spectrin formed random meshwork or repeated structures in dendritic shafts and filopodial bases. It has previously been demonstrated using young hippocampal neurons that the transition from filopodia to neurites is triggered by microtubule invasion into the filopodia following local actin remodeling (Dent et al., 2007; Flynn et al., 2012). To test whether  $\beta$ III spectrin contributes to blocking microtubule entry into dendritic protrusions, we monitored microtubule polymerization in growing dendrites via transfection with EB3-EGFP, a plus-end marker of dynamic microtubules fused with EGFP. We analyzed the growing terminals of dendrites (within  $10 \mu\text{m}$  from the terminal) and more proximal dendrites (more than  $10 \mu\text{m}$  away from the terminal) separately to examine the regional difference in EB3 dynamics.

In ctr cells,  $48 \pm 5\%$  (mean  $\pm$  SEM, 226 protrusions from 18 dendrites) of dendritic protrusions around the growing terminal were targeted by EB3-EGFP within 150 seconds of observation (Figs. 7A and C). In contrast, a significantly lower proportion of protrusions were invaded by EB3 in proximal dendrites ( $5 \pm 2\%$ , 149 protrusions from 11 dendrites, ctr distal vs ctr proximal,  $p = 1.3 \times 10^{-4}$ , Kruskal-Wallis followed by Steel-Dwass test), in line with the notion that microtubule entry into filopodia triggers neurite extension. We found that  $\beta$ III spectrin knockdown significantly increased the proportion of EB3-targeted protrusions in proximal regions ( $41 \pm 6\%$ , 91 protrusions from 10 dendrites, ctr proximal vs  $\beta$ III kd proximal,  $p = 1.0 \times 10^{-3}$ ) (Figs. 7B and C), while only a slight increase was observed in the distal area ( $67 \pm 4\%$ , 102 protrusions from 13 dendrites, ctr distal vs  $\beta$ III kd distal,  $p = 0.08$ ). These data support the idea that  $\beta$ III spectrin interferes with microtubule invasion into dendritic protrusions in proximal dendrites. Furthermore, we often observed that EB3-positive puncta guided the filopodia and promoted their aberrant extension in  $\beta$ III spectrin kd cells (Fig. 7D). The speed of microtubule polymerization was instead slightly downregulated in  $\beta$ III spectrin-knockdown cells (distal; ctr:  $0.119 \pm 0.002 \mu\text{m}/\text{sec}$  vs  $\beta$ III kd:  $0.101 \pm 0.002 \mu\text{m}/\text{sec}$ , proximal; ctr:  $0.129 \pm 0.003 \mu\text{m}/\text{sec}$  vs

$\beta$ III kd:  $0.101 \pm 0.002 \mu\text{m}/\text{sec}$ , mean  $\pm$  SEM), demonstrating that excessive microtubule entry in  $\beta$ III spectrin-deficient cells was not due to increased microtubule polymerization activity (Fig. 7E). Thus, these results suggest that  $\beta$ III spectrin steers directed dendritic growth by suppressing microtubule invasion and ectopic branch formation from proximal dendritic protrusions (Fig. 7F).

### **Mutations causing spinocerebellar ataxia type 5 (SCA5)**

Mutations in  $\beta$ III spectrin are known to cause spinocerebellar ataxia type 5 (SCA5). Hence, we wondered if the disease mutations affect biased dendrite growth perpendicular to GC axons. We focused on three mutations identified in earlier studies (Fig. 8A) (Ikeda et al., 2006). The first is a point mutation found in German families that results in a leucine to proline substitution (L253P) in the calponin homology domain; the second is an in-frame 39-bp (13-amino acid) deletion (E532-M544 del) in the third spectrin repeat found in American families; and the third is a 15-bp deletion in the third spectrin repeat (5-amino acid deletion with the insertion of tryptophan, L629-R634 delinsW) found in French families (Fig. 8A). The amino acid sequences related to these disease mutations are conserved among humans and mice. Thus, we generated mouse  $\beta$ III spectrin mutant constructs harboring the corresponding mutations. These constructs were designed to be shRNA resistant and were tagged with a myc epitope at their N-termini for imaging.

We knocked down endogenous  $\beta$ III spectrin and performed co-transfection with wild-type  $\beta$ III spectrin or disease-related mutants in dissociated PCs on aligned nanofiber substrates. Wild-type  $\beta$ III spectrin was distributed in the somatodendritic area up to the most distal dendritic regions. In sharp contrast, the L253P mutant form was localized in intracellular vesicular structures in the somatic area, while almost no signal was observed in the dendrites (Fig. 8B). On the other hand, mutants with deletions in the third spectrin repeat (E532-M544 del and L629-R634 delinsW) localized to the dendritic plasma membrane to a lesser extent than wild-type molecules. Quantitative image analysis revealed the differential localization of mutants in PC dendrites (Fig. 8C).

PCs expressing the shRNA-resistant wild-type molecule exhibited normal perpendicular dendrites. However, all disease mutants were defective in the steering of perpendicular dendrite growth. L253P and E532-M544 were completely incompetent in perpendicular guidance, while the L629-R634 delinsW mutation, which showed modest mislocalization, retained weak but significant guidance activity (Fig. 8D). These results suggest that some disease mutations of  $\beta$ III spectrin disrupt dendritic configuration in PCs.

## Discussion

In this study, we show that  $\beta$ III spectrin is required for the directed dendrite growth of PCs in the perpendicular direction with respect to parallel fiber axons, which is important for the formation of planar dendrites *in vivo*. The loss of  $\beta$ III spectrin causes ectopic branch formation, extending away from the main sagittal dendritic plane.  $\beta$ III spectrin forms membrane-associated skeletal structures along the dendritic shaft and at the base of dendritic protrusions in PCs. In the absence of  $\beta$ III spectrin, microtubules aberrantly enter dendritic protrusions in proximal dendrites, probably leading to the formation of abnormally oriented dendrites. We propose that  $\beta$ III spectrin serves as a molecular fence confining the distribution of actin and microtubules across dendritic protrusions and dendritic shafts.

### Biased dendrite growth perpendicular to axonal bundles and planar dendrite formation

We established a 2D model of axon-dendrite topology using aligned nanofibers and confirmed that PC dendrites grew preferentially in the direction perpendicular to the bundles of afferent parallel fiber axons. The perpendicular interactions may serve as a permissive mechanism for the planar arborization of Purkinje cell dendrites in parasagittal planes. Indeed, earlier studies demonstrated that the disruption of parallel fiber arrays via the X-ray irradiation of the developing cerebellum led to the realignment of PC dendrites in a direction perpendicular to the misoriented parallel fibers. However, other mechanisms should also be involved in the spatial organization of PC dendrites, as perpendicular contacts would not assure arborization in the exact parasagittal plane. For instance, contact-based repulsion may support the formation of flat dendrites by regulating the space between neighboring dendritic planes (Fig. 5A).

### Dendrite growth dynamics and $\beta$ III spectrin

In the present study, we demonstrate that the cell-autonomous function of  $\alpha$ II and  $\beta$ III spectrins in PCs is required for directed branch growth and flat dendrite organization. Time-lapse observations and confocal microscopy analysis of tissue and cultures revealed aberrant branch formation resulting from the loss of  $\beta$ III spectrin. The dendrites of developing PCs in culture exhibit numerous lateral protrusions expressing the postsynaptic protein GluD2, suggesting that these protrusions are immature spine precursors. In ctr PCs, dendritic branches are formed mainly by terminal bifurcation, with only a few collateral branches forming from proximal dendrites. In contrast, lateral branching events are significantly increased in  $\beta$ III spectrin kd cells (Fig. 4G). Furthermore,  $\beta$ III spectrin kd dendrites exhibit protrusions that are irregularly arranged and vary in size: some protrusions abnormally extend to a length indistinguishable from that of dendritic branches. Thus, the loss of  $\beta$ III spectrin seems to alter the fate of proximal dendritic protrusions

from immature spines to branch precursors, which become misoriented branches extruded from the main parasagittal plane (Fig. 5).

GluD2 was found to mislocalize along the elongated protrusions and shafts of  $\beta$ III spectrin kd dendrites, consistent with previous observations (Gao et al., 2011). GluD2 has been shown to function as a synaptic glue and anchor spines to presynaptic terminals (Matsuda et al., 2010; Uemura et al., 2010). We assume that the regularly arranged lateral protrusions might tightly associate with parallel fibers via GluD2-neurexin interaction and hold the dendrite stems on parallel fibers at right angles. In contrast, ectopic GluD2 in the dendrites and protrusions of  $\beta$ III spectrin kd cells may adhere to parallel fibers at incorrect positions and thereby misorient dendrite growth.

### **SCA5-related mutations affect dendrite growth in PCs**

We demonstrate that disease mutations related to SCA5 affect oriented dendrite formation in PCs on nanofibers (Fig. 8). Previous studies using *Drosophila* dendrite arborization (DA) neurons showed that the L253P-type mutation in *Drosophila*  $\beta$ -spectrin causes defects in dendritic development (Avery et al., 2017). The L253P mutation has been shown to increase the affinity for actin filaments while downregulating  $\beta$ -spectrin binding to actin-related protein 1 (Arp1, a component of the dynactin complex)(Avery et al., 2016; Clarkson et al., 2010). Consistent with previous studies showing that the L253P mutation affects the trafficking of  $\beta$ -spectrin from the Golgi apparatus (Clarkson et al., 2010), we observed that L253P mutant proteins accumulate at intracellular vesicular structures in PC somata. L253P mutant proteins are not delivered to dendritic membranes nor do they replace the function of wild-type molecules in guiding the oriented growth of PC dendrites. In contrast, the L629-R634 delinsW mutation has only minor effects on dendritic localization and the oriented growth of dendrites. Interestingly, the E532-M544 del mutant is severely defective in guiding dendrite growth orientation despite its relatively normal dendritic localization, except in the distalmost region. It has been proposed that the deletion of E532-M544 possibly affects the triple alpha-helical structures of the spectrin repeats, which might result in the alteration of overall alpha/beta structures (Ikeda et al., 2006). We assume that the E532-M544 del mutation may retard the stabilization of the newly formed spectrin architecture in the distal growing region of the dendrites and interfere with dendrite growth in the normal direction.

### **Microtubule dynamics and dendritic branching**

Neurite formation and branching are known to require microtubule extension into precursor protrusions or filopodia (Burnette et al., 2007; Dent et al., 2007; Flynn et al., 2012; Hu et al., 2012). Flynn et al proposed that neurite initiation is triggered by the ADF/cofilin-induced

destabilization of cortical actin filaments, which leads to the disassembly of the dense actin meshwork and microtubule entry into the emerging process. It is thought that bundled actin in filopodia guides microtubules into filopodial protrusions (Dent et al., 2007). In contrast, the cortical actin meshwork confines microtubules in the shaft region and suppresses the interaction between microtubules and bundled actin filaments in filopodial protrusions. We observed frequent microtubule invasion almost exclusively in distal protrusions in normal PCs, supporting the idea that microtubule invasion triggers branch growth in PC dendrites, which predominantly extend at the distal ends. On the other hand, polymerizing microtubules enter the proximal protrusions more frequently and promote their abnormal elongation in  $\beta$ III spectrin kd PCs (Fig. 7).  $\beta$ III spectrin is enriched in the thin neck regions of dendritic protrusions, and its loss sometimes leads to the formation of stubby protrusions (Fig. 6J, type 2), supporting the involvement of  $\beta$ III spectrin in neck formation. It is thus suggested that the cortical membrane skeleton containing  $\beta$ III spectrin might cooperate with cortical actin and function as a molecular fence confining microtubule dynamics along dendrites.

In mature dendrites, neuronal activity facilitates microtubule invasion into dendritic spines (Gu et al., 2008; Jaworski et al., 2009; Merriam et al., 2013). It has been proposed that neuronal activity increases the formation of the actin cytoskeleton at the base of the spines, which directly guide the entry of microtubules into the spines (Schätzle et al., 2018). In  $\beta$ III spectrin-deficient PCs, actin signals at the tip of protrusions expand within the protrusion base and dendritic shaft. The ectopic localization of actin might increase collisions with microtubules in the shaft, promoting microtubule entry into the protrusions. Alternatively, spectrin molecules may interact with other microtubule-associated proteins, such as 4.1R (Huang et al., 2004; Ruiz-Saenz et al., 2013) and ankyrins (Fréal et al., 2016; Leterrier et al., 2011; Yang et al., 2019). The elucidation of the precise mechanisms of the interaction of spectrin with other cytoskeletal proteins in growing dendrites must await further studies.

### **Significance of perpendicular contact between axons and dendrites.**

What is the biological significance of the unique topology of flat PC dendrites that cross vertically to parallel fiber axons? First, the topology of axon-dendrite contacts is thought to be important for efficient network formation. In general, neuronal circuits in the animal brain are thought to evolve to maximize brain functionality while minimizing metabolic costs attributed to neurite volume (Bullmore and Sporns, 2012; Wang and Clandinin, 2016). The perpendicular arrangement of dendrites and axons would maximize the number of physical contacts in a given dendritic length. Indeed, flat PC dendrites have been demonstrated to present the most efficient geometrical arrangement for neuronal connectivity (Cuntz, 2012; Wen and Chklovskii, 2008). Second, dendritic planarity is necessary to minimize redundant connectivity with parallel fiber arrays

(Fujishima et al., 2018; Han et al., 2012; Kim et al., 2012). Growing PC dendrites adopt a self-avoidance mechanism to avoid crossing with dendritic arbors in a given sagittal plane (Fujishima et al., 2012; Gibson et al., 2014; Lefebvre et al., 2012). In addition to the self-avoidance of sister branches, the present study suggests a mechanism suppressing the formation of three-dimensional dendrites passing above along the coronal axis. Although one should consider the possibility of an as-yet-unidentified mechanism involving other cell types, our observations indicate the cell-autonomous function of  $\beta$ III spectrin as a permissive factor inhibiting coronally oriented branches.

Previous studies using diffusion magnetic resonance imaging have revealed a 3D grid-like organization of axonal bundles in the forebrain, in which two distinct fibers (transverse path and longitudinal path) interweave and cross at nearly right angles (Wedeen et al., 2012). Such a grid-like organization might be formed by perpendicular contact guidance between different types of axons. It is of interest to confirm whether perpendicular contact is a general mechanism in neural network formation.

## Materials and methods

### Antibody list

Rabbit polyclonal anti- $\beta$ III Spectrin	SantaCruz	sc-28273
Goat polyclonal anti- $\beta$ III Spectrin	SantaCruz	sc-9660
Mouse monoclonal anti- $\beta$ III Spectrin	SantaCruz	sc-515737
Mouse monoclonal anti- $\alpha$ II Spectrin	SantaCruz	sc-376849
Rabbit polyclonal anti-GFP	Thermo Fisher Scientific	A-11122
Mouse monoclonal anti-GFP	Thermo Fisher Scientific	A-11120
Rabbit polyclonal anti-RFP	MBL Life Science	PM005
Mouse monoclonal anti-Calbindin	Swant	300
Mouse monoclonal anti-c-Myc	SantaCruz	sc-40
Mouse monoclonal anti-HA	Roche	1583816
Rabbit polyclonal-Pax6	Wako	019-27291
Rabbit polyclonal anti-GluD2-C	Frontier Institute	GluRD2C-Rb-Af500
Mouse monoclonal anti-tau	MERCK	MAB3420
Donkey anti-Mouse Alexa Fluor 488	Thermo Fisher Scientific	A-21202
Donkey anti-Mouse Alexa Fluor 555	Thermo Fisher Scientific	A-31570
Donkey anti-Mouse Alexa Fluor 647	Thermo Fisher Scientific	A-31571
Donkey anti-Rabbit Alexa Fluor 488	Thermo Fisher Scientific	A-21206
Donkey anti-Rabbit Alexa Fluor 555	Thermo Fisher Scientific	A-31572
Donkey anti-Rabbit Alexa Fluor 647	Thermo Fisher Scientific	A-31573
Donkey anti-Goat Alexa Fluor 555	Thermo Fisher Scientific	A-21432
Donkey anti-Goat Alexa Fluor 568	Thermo Fisher Scientific	A-11057
Donkey anti-Goat Alexa Fluor 647	Thermo Fisher Scientific	A-21447

### Mice

Mice were handled in accordance with the guidelines of the Animal Experiment Committee of Kyoto University and were housed in a dedicated pathogen-free environment with a 12-hour light/dark cycle.

### Plasmids

The pAAV-CAG-GFP-hH1 vector, including the human H1 promoter, was used to express shRNA to knock down target gene expression as previously described (Fukumitsu et al., 2015). The targeting sequences were designed by using the web-based software siDirect (Naito et al., 2009): control shRNA (5'-GCATCTCCATTAGCGAACATT-3'),  $\beta$ III-spectrin shRNA (5'-

GTCAATGTGCACAACTTTACC-3'),  $\alpha$ II spectrin shRNA (5'-GTAAAGACCTCACTAATGTCC-3'). To generate resistant mutants of  $\alpha$ II spectrin and  $\beta$ III-spectrin that contained three silent mutations within shRNA target sequences, the cDNA of mouse  $\alpha$ II spectrin or  $\beta$ III-spectrin was cloned from a mouse brain cDNA library and mutagenized by using a PCR-based method. To generate the L253P, E532-M544 del and L629-R634 delinsW  $\beta$ III spectrin mutants, PCR-based mutagenesis was performed by using the resistant mutant of  $\beta$ III-spectrin as a template.  $\alpha$ II spectrin tagged with HA at the N-terminus and  $\beta$ III-spectrin wild-type and mutant sequences tagged with myc at the N-terminus were cloned into the pCAGGS vector. To generate the EB3-EGFP construct, the coding sequence of EB3 was amplified from a mouse brain cDNA library and inserted into the pAAV-CAG-EGFP plasmid. For the CRISPR/Cas9-based knockout of  $\beta$ III-spectrin, the guide RNA sequence was selected by using the web-based software CRISPRdirect (Naito et al., 2015). The  $\beta$ III-spectrin target sequence (5'-GAGACCTGTACAGCGACCTG-3') was inserted into pSpCas9(BB)-2A-GFP (PX458) (Addgene plasmid #48138) (Ran et al., 2013).

### ***In utero electroporation***

The *in utero* electroporation of plasmids was performed as described previously (Nishiyama et al., 2012). Briefly, pregnant mice on day 11.5 of gestation were deeply anesthetized via the intra-abdominal injection of somnopentyl (Kyoritsu). Plasmid DNA (1-5  $\mu$ g/ $\mu$ l) was microinjected into the fourth ventricle of the embryos (FemtoJet; Eppendorf). Then, five current pulses (amplitude, 33 V; duration, 30 ms; intervals, 970 ms) were delivered with a forceps-shaped electrode (CUY650P3; NepaGene) connected to an electroporator (CUY21; NepaGene).

### ***In vivo electroporation to label parallel fibers***

The *in vivo* electroporation of plasmids was performed as described previously (Umeshima et al., 2007). Briefly, P8 ICR mice were cryoanesthetized. A small burr hole was made in the skull over the cerebellum with a 27-gauge needle. The plasmid DNA (pAAV-CAG-mCherry) was microinjected through the hole by using a syringe with a 33-gauge needle (Ito). A forceps-shaped electrode connected to the cathode of an electroporator (CUY21; NepaGene) was placed in the occipital region. A needle used for DNA injection was connected to the anode. Then, six current pulses (amplitude, 70 V; duration, 50 ms; intervals, 150 ms) were delivered. After the wound was sutured, the pups were warmed at 37°C and returned to the home cage.

### **Primary culture and nucleofection of cerebellar neurons**

The primary culture of cerebellar neurons was performed as previously described (Fujishima et al., 2012) with slight modifications. Cerebella from postnatal day (P) 0 mice were dissected in

HBSS (GIBCO) and dissociated using a Neuron Dissociation Kit (FUJIFILM Wako Pure Chemical Corporation). Cells were plated on a 12 mm coverslip coated with poly-D-lysine in DMEM/F12 supplemented with 10% FBS at a density of 1.5 cerebella/coverslip. Following incubation, the media were replaced with maintenance media containing DMEM/F12, 0.1 mg/ml bovine serum albumin, 2.1 mg/ml glucose, 2X Glutamax, 8  $\mu$ M progesterone, 20  $\mu$ g/ml insulin, 200  $\mu$ g/ml transferrin, 100  $\mu$ M putrescine, 30 nM selenium dioxide, 4  $\mu$ M AraC and 1% penicillin-streptomycin. For cultures on nanofibers, dissociated neurons were plated on aligned or random nanofiber plates (Nanofiber solutions).

For the transfection of plasmid DNA into Purkinje cells, nucleofection was performed as described previously (Kawabata Galbraith et al., 2018). Briefly, dissociated cerebellar cells from 1.5-2 cerebella were washed twice with OptiMEM and resuspended in 100  $\mu$ l of OptiMEM containing 5-8  $\mu$ g of plasmid DNA. Cells were transferred to a cuvette and nucleofected with a Nepa21 electroporator (NEPAGENE).

### **Immunofluorescence and image acquisition**

For immunocytochemistry, cells cultured on coverslips or nanofibers were fixed for 15 min at RT in 4% paraformaldehyde (PFA) in PBS. Cells were washed and permeabilized with PBS containing 0.25% Triton (PBS-0.25T). The cells were then blocked with PBS (-0.25 T) with 2% bovine serum albumin (BSA) for 30 min at RT. The cells were incubated with primary antibodies at 4°C overnight in PBS (-0.25 T) with 2% BSA, washed with PBS, and incubated with fluorescently labeled secondary antibodies in PBS (-0.25 T) with 2% BSA.

For immunohistochemistry, the mice were anesthetized with isoflurane and perfused with PBS followed by 4% PFA in phosphate buffer. Their brains were removed and postfixed overnight in 4% PFA/PBS at 4°C. After washing with PBS, the brains were embedded in 3.5% low-melt agarose in PBS. Sagittal or coronal sections were cut at a 50-100  $\mu$ m thickness by using a vibratome (Dosaka). The sections were permeabilized in PBS with 0.5% Triton (PBS-0.5 T) and blocked with 2% skim milk in PBS (-0.5 T) for 30 min. The sections were incubated with primary antibodies at 4°C overnight in blocking solution, washed with PBS, and incubated with fluorescently labeled secondary antibodies in 2% skim milk in PBS (-0.5 T).

### **Quantification of dendrite morphology**

For the analysis of dendritic flatness, captured confocal 3D images were binarized and skeletonized in ImageJ ("*Skeletonize (2D/3D)*" plugin). To identify the plane with the closest fit to the given dendritic arbor, principal component analysis was performed in MATLAB software. To analyze the distance of the dendritic branches from the fitted plane, 3000 points (for Figs. 1A and B) or 100 points (for Fig. 1D) in the skeletonized dendritic images from each cell were

randomly selected, and the distance between each point and the fitted plane was calculated.

For the morphometric analysis of PC dendrites on aligned fibers, Z-projected images were binarized and skeletonized in the ImageJ plugin or MATLAB software. To analyze the branch angle, dendritic branches were divided into 3.5  $\mu\text{m}$  segments, and the angle between each segment and fiber was quantified.

### **STED imaging**

We used a Leica TCS SP8 STED with an oil immersion 100x objective lens with NA 1.4 (HC-PL-APO 100x/1.4 OIL, Leica) to analyze the subcellular localization of  $\beta\text{III}$  spectrin. The protein was labeled with anti- $\beta\text{III}$  spectrin (Santa Cruz, SC-28273) and a secondary antibody conjugated with Alexa555 (Thermo Fisher). The fluorophore was excited with a white laser tuned to 555 nm and depleted with a 660 nm STED laser. A time gate window of 0.35-3.85 ns was used to maximize the STED resolution.

### **Time-lapse imaging, image processing, and image analysis**

For long-term time-lapse imaging, fluorescently labeled Purkinje cells were observed every 1-3 hours with an incubation microscope (LCV100, Olympus) equipped with a 20x objective (NA 0.7, Olympus). Serial z-stacked images were obtained at z-steps of 1  $\mu\text{m}$  (1  $\mu\text{m}$  x 5 steps).

For the high-resolution live imaging of dendritic arbors (used for EB3 imaging experiments), images were obtained with a confocal microscope (FV1000, BX61W1; Olympus) equipped with a LUMFI 60x objective (NA 1.10, Olympus) under 5%  $\text{CO}_2$  supplementation. Images were recorded with 3x digital zoom at an interval of 3 s.

For the analysis of EB3 dynamics, average subtraction was performed to eliminate background cytosolic signals (Schätzle et al., 2016). Briefly, an average projection of all of the time-lapse images of EB-EGFP signals was generated and subtracted from each frame of the time-lapse images. The images were then processed via an unsharp masking procedure in ImageJ software to obtain the enhanced images. The dynamics of EB3-EGFP were tracked by using the ImageJ plugin “TrackMate”, and the number of filopodial invasions of EB3 was calculated.

## Acknowledgements

We thank iCeMS Analysis Center and Dr. Yukiko Ohara for technical assistance. This work was supported by KAKENHI grants from the Japan Society for the Promotion of Science (JSPS) (#16H06484 and #17K19453 to MK, #16K18363 and #16KT0171 to KF) and Takeda Science Foundation to KF.

## Author Contributions

Conceptualization, K.F. and M.K.; Methodology, K.F. and M.K.; Investigation, K.F., J.K. and M.Y.; Formal analysis, K.F., J.K. and M.Y.; Writing K.F. and M.K.

## Declaration of Interests

The authors declare no competing interests.

## References

- Albrecht, D., Winterflood, C.M., Sadeghi, M., Tschager, T., Noé, F., and Ewers, H. (2016). Nanoscopic compartmentalization of membrane protein motion at the axon initial segment. *J Cell Biol* 215, 37–46.
- Armbrust, K.R., Wang, X., Hathorn, T.J., Cramer, S.W., Chen, G., Zu, T., Kangas, T., Zink, A.N., Öz, G., Ebner, T.J., et al. (2014). Mutant  $\beta$ -III Spectrin Causes mGluR1 $\alpha$  Mislocalization and Functional Deficits in a Mouse Model of Spinocerebellar Ataxia Type 5. *J. Neurosci.* 34, 9891–9904.
- Avery, A.W., Crain, J., Thomas, D.D., and Hays, T.S. (2016). A human  $\beta$ -III-spectrin spinocerebellar ataxia type 5 mutation causes high-affinity F-actin binding. *Sci. Rep.* 6, 21375.
- Avery, A.W., Thomas, D.D., and Hays, T.S. (2017).  $\beta$ -III-spectrin spinocerebellar ataxia type 5 mutation reveals a dominant cytoskeletal mechanism that underlies dendritic arborization. *Proc. Natl. Acad. Sci.* 114, E9376–E9385.
- Bullmore, E., and Sporns, O. (2012). The economy of brain network organization. *Nat. Rev. Neurosci.* 13, 336–349.
- Burnette, D.T., Schaefer, A.W., Ji, L., Danuser, G., and Forscher, P. (2007). Filopodial actin bundles are not necessary for microtubule advance into the peripheral domain of *Aplysia* neuronal growth

cones. *Nat. Cell Biol.* 9, 1360–1369.

Chen, C.-H., Hsu, H.-W., Chang, Y.-H., and Pan, C.-L. (2019). Adhesive L1CAM-Robo Signaling Aligns Growth Cone F-Actin Dynamics to Promote Axon-Dendrite Fasciculation in *C. elegans*. *Dev. Cell* 48, 215-228.e5.

Cianci, C.D., Zhang, Z., Pradhan, D., and Morrow, J.S. (1999). Brain and Muscle Express a Unique Alternative Transcript of  $\alpha$ II Spectrin. *Biochemistry* 38, 15721–15730.

Cioni, J.-M., Wong, H.H.-W., Bressan, D., Kodama, L., Harris, W.A., and Holt, C.E. (2018). Axon-Axon Interactions Regulate Topographic Optic Tract Sorting via CYFIP2-Dependent WAVE Complex Function. *Neuron* 97, 1078-1093.e6.

Clarkson, Y.L., Gillespie, T., Perkins, E.M., Lyndon, A.R., and Jackson, M. (2010).  $\beta$ -III spectrin mutation L253P associated with spinocerebellar ataxia type 5 interferes with binding to Arp1 and protein trafficking from the Golgi. *Hum. Mol. Genet.* ddq279.

Cuntz, H. (2012). The dendritic density field of a cortical pyramidal cell. *Front. Neuroanat.* 6, 2.

Dent, E.W., Kwiatkowski, A.V., Mebane, L.M., Philippar, U., Barzik, M., Robinson, D.A., Gupton, S., Van Veen, J.E., Furman, C., Zhang, J., et al. (2007). Filopodia are required for cortical neurite initiation. *Nat. Cell Biol.* 9, 1347–1359.

D’Este, E., Kamin, D., Göttfert, F., El-Hady, A., and Hell, S.W. (2015). STED Nanoscopy Reveals the Ubiquity of Subcortical Cytoskeleton Periodicity in Living Neurons. *Cell Rep.* 10, 1246–1251.

Efimova, N., Korobova, F., Stankewich, M.C., Moberly, A.H., Stolz, D.B., Wang, J., Kashina, A., Ma, M., and Svitkina, T. (2017).  $\beta$ III Spectrin Is Necessary for Formation of the Constricted Neck of Dendritic Spines and Regulation of Synaptic Activity in Neurons. *J. Neurosci.* 37, 6442–6459.

Flynn, K.C., Hellal, F., Neukirchen, D., Jacob, S., Tahirovic, S., Dupraz, S., Stern, S., Garvalov, B.K., Gurniak, C., Shaw, A.E., et al. (2012). ADF/Cofilin-Mediated Actin Retrograde Flow Directs Neurite Formation in the Developing Brain. *Neuron* 76, 1091–1107.

Fréal, A., Fassier, C., Bras, B.L., Bullier, E., Gois, S.D., Hazan, J., Hoogenraad, C.C., and Couraud, F. (2016). Cooperative Interactions between 480 kDa Ankyrin-G and EB Proteins Assemble the Axon Initial Segment. *J. Neurosci.* 36, 4421–4433.

Fujishima, K., Horie, R., Mochizuki, A., and Kengaku, M. (2012). Principles of branch dynamics governing shape characteristics of cerebellar Purkinje cell dendrites. *Development* 139, 3442–3455.

Fujishima, K., Kawabata Galbraith, K., and Kengaku, M. (2018). Dendritic Self-Avoidance and Morphological Development of Cerebellar Purkinje Cells. *The Cerebellum* 17, 701–708.

Fukumitsu, K., Fujishima, K., Yoshimura, A., Wu, Y.K., Heuser, J., and Kengaku, M. (2015). Synergistic action of dendritic mitochondria and creatine kinase maintains ATP homeostasis and actin dynamics in growing neuronal dendrites. *J. Neurosci.* 35, 5707–5723.

Gao, Y., Perkins, E.M., Clarkson, Y.L., Tobia, S., Lyndon, A.R., Jackson, M., and Rothstein, J.D. (2011). B-III spectrin is critical for development of Purkinje cell dendritic tree and spine morphogenesis. *J. Neurosci.* 31, 16581–16590.

Gibson, D.A., Tymanskyj, S., Yuan, R.C., Leung, H.C., Lefebvre, J.L., Sanes, J.R., Chédotal, A., and Ma, L. (2014). Dendrite self-avoidance requires cell-autonomous slit/robo signaling in cerebellar Purkinje cells. *Neuron* 81, 1040–1056.

Grueber, W.B., and Sagasti, A. (2010). Self-avoidance and tiling: Mechanisms of dendrite and axon spacing. *Cold Spring Harb. Perspect. Biol.* 2, a001750.

Gu, J., Firestein, B.L., and Zheng, J.Q. (2008). Microtubules in Dendritic Spine Development. *J. Neurosci.* 28, 12120–12124.

Han, B., Zhou, R., Xia, C., and Zhuang, X. (2017). Structural organization of the actin-spectrin-based membrane skeleton in dendrites and soma of neurons. *Proc. Natl. Acad. Sci.* 114, E6678–E6685.

Han, C., Wang, D., Soba, P., Zhu, S., Lin, X., Jan, L.Y., and Jan, Y.-N. (2012). Integrins regulate repulsion-mediated dendritic patterning of *Drosophila* sensory neurons by restricting dendrites in a 2D space. *Neuron* 73, 64–78.

Hayashi, S., Inoue, Y., Kiyonari, H., Abe, T., Misaki, K., Moriguchi, H., Tanaka, Y., and Takeichi, M. (2014). Protocadherin-17 Mediates Collective Axon Extension by Recruiting Actin Regulator Complexes to Interaxonal Contacts. *Dev. Cell* 30, 673–687.

Hu, J., Bai, X., Bowen, J.R., Dolat, L., Korobova, F., Yu, W., Baas, P.W., Svitkina, T., Gallo, G., and Spiliotis, E.T. (2012). Septin-Driven Coordination of Actin and Microtubule Remodeling Regulates the Collateral Branching of Axons. *Curr. Biol.* 22, 1109–1115.

Huang, S.-C., Jagadeeswaran, R., Liu, E.S., and Benz, E.J. (2004). Protein 4.1R, a Microtubule-associated Protein Involved in Microtubule Aster Assembly in Mammalian Mitotic Extract. *J. Biol. Chem.* 279, 34595–34602.

- Hyysalo, A., Ristola, M., Joki, T., Honkanen, M., Vippola, M., and Narkilahti, S. (2017). Aligned Poly( $\epsilon$ -caprolactone) Nanofibers Guide the Orientation and Migration of Human Pluripotent Stem Cell-Derived Neurons, Astrocytes, and Oligodendrocyte Precursor Cells In Vitro. *Macromol. Biosci.* *17*, 1600517.
- Ikeda, Y., Dick, K.A., Weatherspoon, M.R., Gincel, D., Armbrust, K.R., Dalton, J.C., Stevanin, G., Dürr, A., Zühlke, C., Bürk, K., et al. (2006). Spectrin mutations cause spinocerebellar ataxia type 5. *Nat. Genet.* *38*, 184–190.
- Jaworski, J., Kapitein, L.C., Gouveia, S.M., Dortland, B.R., Wulf, P.S., Grigoriev, I., Camera, P., Spangler, S.A., Di Stefano, P., Demmers, J., et al. (2009). Dynamic Microtubules Regulate Dendritic Spine Morphology and Synaptic Plasticity. *Neuron* *61*, 85–100.
- Kawabata Galbraith, K., Fujishima, K., Mizuno, H., Lee, S.-J., Uemura, T., Sakimura, K., Mishina, M., Watanabe, N., and Kengaku, M. (2018). MTSS1 Regulation of Actin-Nucleating Formin DAAM1 in Dendritic Filopodia Determines Final Dendritic Configuration of Purkinje Cells. *Cell Rep.* *24*, 95-106.e9.
- Kim, M.E., Shrestha, B.R., Blazeski, R., Mason, C.A., and Grueber, W.B. (2012). Integrins establish dendrite-substrate relationships that promote dendritic self-avoidance and patterning in *Drosophila* sensory neurons. *Neuron* *73*, 79–91.
- Krieg, M., Stühmer, J., Cueva, J.G., Fetter, R., Spilker, K., Cremers, D., Shen, K., Dunn, A.R., and Goodman, M.B. (2017). Genetic defects in  $\beta$ -spectrin and tau sensitize *C. elegans* axons to movement-induced damage via torque-tension coupling. *ELife* *6*, e20172.
- Lefebvre, J.L. (2017). Neuronal territory formation by the atypical cadherins and clustered protocadherins. *Semin. Cell Dev. Biol.* *69*, 111–121.
- Lefebvre, J.L., Kostadinov, D., Chen, W.V., Maniatis, T., and Sanes, J.R. (2012). Protocadherins mediate dendritic self-avoidance in the mammalian nervous system. *Nature* *488*, 517–521.
- Leite, S.C., Sampaio, P., Sousa, V.F., Nogueira-Rodrigues, J., Pinto-Costa, R., Peters, L.L., Brites, P., and Sousa, M.M. (2016). The Actin-Binding Protein  $\alpha$ -Adducin Is Required for Maintaining Axon Diameter. *Cell Rep.* *15*, 490–498.
- Leterrier, C., Vacher, H., Fache, M.-P., d’Ortoli, S.A., Castets, F., Autillo-Touati, A., and Dargent, B. (2011). End-binding proteins EB3 and EB1 link microtubules to ankyrin G in the axon initial segment. *Proc. Natl. Acad. Sci.* *108*, 8826–8831.

Matsuda, K., Miura, E., Miyazaki, T., Kakegawa, W., Emi, K., Narumi, S., Fukazawa, Y., Ito-Ishida, A., Kondo, T., Shigemoto, R., et al. (2010). Cbln1 Is a Ligand for an Orphan Glutamate Receptor  $\delta 2$ , a Bidirectional Synapse Organizer. *Science* 328, 363–368.

Merriam, E.B., Millette, M., Lombard, D.C., Saengsawang, W., Fothergill, T., Hu, X., Ferhat, L., and Dent, E.W. (2013). Synaptic Regulation of Microtubule Dynamics in Dendritic Spines by Calcium, F-Actin, and Drebrin. *J. Neurosci.* 33, 16471–16482.

Nagata, I., Ono, K., Kawana, A., and Kimura-Kuroda, J. (2006). Aligned neurite bundles of granule cells regulate orientation of Purkinje cell dendrites by perpendicular contact guidance in two-dimensional and three-dimensional mouse cerebellar cultures. *J. Comp. Neurol.* 499, 274–289.

Naito, Y., Yoshimura, J., Morishita, S., and Ui-Tei, K. (2009). siDirect 2.0: updated software for designing functional siRNA with reduced seed-dependent off-target effect. *BMC Bioinformatics* 10, 392.

Naito, Y., Hino, K., Bono, H., and Ui-Tei, K. (2015). CRISPRdirect: software for designing CRISPR/Cas guide RNA with reduced off-target sites. *Bioinformatics* 31, 1120–1123.

Napper, R.M., and Harvey, R.J. (1988). Number of parallel fiber synapses on an individual Purkinje cell in the cerebellum of the rat. *J. Comp. Neurol.* 274, 168–177.

Nishiyama, J., Hayashi, Y., Nomura, T., Miura, E., Kakegawa, W., and Yuzaki, M. (2012). Selective and regulated gene expression in murine Purkinje cells by in utero electroporation. *Eur. J. Neurosci.* 36, 2867–2876.

Perkins, E.M., Clarkson, Y.L., Sabatier, N., Longhurst, D.M., Millward, C.P., Jack, J., Toraiwa, J., Watanabe, M., Rothstein, J.D., Lyndon, A.R., et al. (2010). Loss of  $\beta$ -III Spectrin Leads to Purkinje Cell Dysfunction Recapitulating the Behavior and Neuropathology of Spinocerebellar Ataxia Type 5 in Humans. *J. Neurosci.* 30, 4857–4867.

Ramirez-Suarez, N.J., Belalcazar, H.M., Salazar, C.J., Beyaz, B., Raja, B., Nguyen, K.C.Q., Celestrin, K., Fredens, J., Færgeman, N.J., Hall, D.H., et al. (2019). Axon-Dependent Patterning and Maintenance of Somatosensory Dendritic Arbors. *Dev. Cell* 48, 229–244.e4.

Ran, F.A., Hsu, P.D., Wright, J., Agarwala, V., Scott, D.A., and Zhang, F. (2013). Genome engineering using the CRISPR-Cas9 system. *Nat. Protoc.* 8, 2281–2308.

Ruiz-Saenz, A., Haren, J. van, Sayas, C.L., Rangel, L., Demmers, J., Millán, J., Alonso, M.A., Galjart, N., and Correas, I. (2013). Protein 4.1R binds to CLASP2 and regulates dynamics, organization and

attachment of microtubules to the cell cortex. *J Cell Sci* 126, 4589–4601.

Schätzle, P., Kapitein, L.C., and Hoogenraad, C.C. (2016). Chapter 4 - Live imaging of microtubule dynamics in organotypic hippocampal slice cultures. In *Methods in Cell Biology*, K.K. Pfister, ed. (Academic Press), pp. 107–126.

Schätzle, P., Silva, M.E. da, Tas, R.P., Katrukha, E.A., Hu, H.Y., Wierenga, C.J., Kapitein, L.C., and Hoogenraad, C.C. (2018). Activity-Dependent Actin Remodeling at the Base of Dendritic Spines Promotes Microtubule Entry. *Curr. Biol.* 0.

Shimada, A., Mason, C.A., and Morrison, M.E. (1998). TrkB Signaling Modulates Spine Density and Morphology Independent of Dendrite Structure in Cultured Neonatal Purkinje Cells. *J. Neurosci.* 18, 8559–8570.

Stankewich, M.C., Gwynn, B., Ardito, T., Ji, L., Kim, J., Robledo, R.F., Lux, S.E., Peters, L.L., and Morrow, J.S. (2010). Targeted deletion of  $\beta$ III spectrin impairs synaptogenesis and generates ataxic and seizure phenotypes. *Proc. Natl. Acad. Sci.* 107, 6022–6027.

Stankewich, M.C., Cianci, C.D., Stabach, P.R., Ji, L., Nath, A., and Morrow, J.S. (2011). Cell organization, growth, and neural and cardiac development require  $\alpha$ II-spectrin. *J Cell Sci* 124, 3956–3966.

Uemura, T., Lee, S.-J., Yasumura, M., Takeuchi, T., Yoshida, T., Ra, M., Taguchi, R., Sakimura, K., and Mishina, M. (2010). Trans-Synaptic Interaction of GluR $\delta$ 2 and Neurexin through Cbln1 Mediates Synapse Formation in the Cerebellum. *Cell* 141, 1068–1079.

Umeshima, H., Hirano, T., and Kengaku, M. (2007). Microtubule-based nuclear movement occurs independently of centrosome positioning in migrating neurons. *Proc. Natl. Acad. Sci.* 104, 16182–16187.

Vassilopoulos, S., Gibaud, S., Jimenez, A., Caillol, G., and Leterrier, C. (2019). Ultrastructure of the axonal periodic scaffold reveals a braid-like organization of actin rings. *Nat. Commun.* 10, 1–13.

Wang, I.E., and Clandinin, T.R. (2016). The Influence of Wiring Economy on Nervous System Evolution. *Curr. Biol.* 26, R1101–R1108.

Wedeen, V.J., Rosene, D.L., Wang, R., Dai, G., Mortazavi, F., Hagmann, P., Kaas, J.H., and Tseng, W.-Y.I. (2012). The Geometric Structure of the Brain Fiber Pathways. *Science* 335, 1628–1634.

Wen, Q., and Chklovskii, D.B. (2008). A Cost-Benefit Analysis of Neuronal Morphology. *J*

Neurophysiol 99, 2320–2328.

Winkelmann, J.C., and Forget, B.G. (1993). Erythroid and nonerythroid spectrins. *Blood* 81, 3173–3185.

Xu, K., Zhong, G., and Zhuang, X. (2013). Actin, Spectrin, and Associated Proteins Form a Periodic Cytoskeletal Structure in Axons. *Science* 339, 452–456.

Yang, R., Walder-Christensen, K.K., Kim, N., Wu, D., Lorenzo, D.N., Badea, A., Jiang, Y.-H., Yin, H.H., Wetsel, W.C., and Bennett, V. (2019). ANK2 autism mutation targeting giant ankyrin-B promotes axon branching and ectopic connectivity. *Proc. Natl. Acad. Sci.* 116, 15262–15271.

## Figure legends

### Figure 1 A Cell-autonomous role of $\beta$ III spectrin in the planar dendrite formation of PCs *in vivo*

(A, B) Representative images of cerebellar Purkinje cells expressing the GFP/shRNA-ctr (A) or GFP/shRNA- $\beta$ III plasmid (B) at P14 in sagittal cerebellar slices. The plasmids were delivered by *in utero* electroporation at E11.5. Top, front (sagittal) and side (coronal) views were taken from the three-dimensionally reconstructed images in Imaris software. Histograms showing the proportions of dendritic segments located at the indicated distances from a plane fitted to the dendrites. Each histogram represents the value measured from a single PC. (C) Quantification of total dendritic length from ctr or  $\beta$ III kd PCs at P14.  $n = 22$  for ctr and  $27$  for  $\beta$ III kd.  $p = 0.67$ , Welch's t-test. (D) Histograms showing the proportions of dendritic segments located at the indicated distances from a plane fitted to the dendrites.  $n = 22$  for ctr and  $n = 27$  for  $\beta$ III kd.  $p = 2.3 \times 10^{-47}$ , two-sample Kolmogorov-Smirnov test. Scale bars:  $20 \mu\text{m}$

### Figure 2 Reconstruction of perpendicular interactions between PC dendrites and GC axons using artificial nanofibers

(A) Purkinje cells (calbindin, green) and parallel fibers (mCherry, magenta, introduced by *in vivo* electroporation) in coronal sections of the P11 cerebellum. (B) Schematic illustrations showing the arrangement of PC dendrites (green) and parallel fibers (GC axons, magenta) in cerebellar tissue and a corresponding 2D model. In tissue, the dendrite of a PC arborizes in a parasagittal plane perpendicular to the bundle of parallel fibers (left cerebellar tissue). In the 2D model, it is hypothesized that PC dendrites may preferentially grow perpendicularly to parallel-oriented GC axons in a two-dimensional culture dish. (C-F) Representative images of GCs (C, E) and PCs (D, F) grown on artificial nanofibers (C, D: aligned and E, F: random). In (C) and (E), Pax6 (green)-positive GC morphologies were visualized with GFP (magenta). Axonal bundles were stained with tau (white). In (D) and (F), Purkinje cell morphologies were visualized by calbindin staining. Axonal bundles (mostly composed of granule cell axons) were stained with tau. The right panels indicate the angular distribution of the axons or dendrites of GCs or PCs on random fibers or aligned fibers. The mean vector is shown with the yellow arrow, and its length is indicated as  $r$ . Scale bars:  $30 \mu\text{m}$

### Figure 3 Disruption of perpendicular dendrite growth via the knockdown of $\beta$ III spectrin

(A) Representative images of PCs transfected with GFP/shRNA control (left panels, ctr), GFP/shRNA- $\beta$ III spectrin (middle panels,  $\beta$ III kd) and GFP/shRNA- $\beta$ III spectrin together with shRNA-resistant  $\beta$ III spectrin (right panels,  $\beta$ III kd + rescue). Cells were grown on aligned fiber substrates and fixed at 12 DIV.  $\beta$ III spectrin signals are shown in magenta. Traced dendrites are pseudocolored based on the

angle between the dendritic segments and fibers. The angular distributions of dendritic segments are indicated by the polar histogram. The mean vector is indicated as  $r$ .  $p = 6 \times 10^{-16}$  for ctr vs  $\beta$ III kd,  $p > 0.5$  for ctr vs rescue, and  $p = 6 \times 10^{-16}$  for  $\beta$ III kd vs rescue according to the Watson-Wheeler test with Bonferroni correction. **(B and C)** Quantification of total dendritic length (B) and the total number of branch points (C) in ctr or  $\beta$ III kd PCs at 12 DIV. Statistical significance was evaluated by ANOVA followed by the Tukey-Kramer post hoc test. **(D)** Representative images of PCs transfected with GFP/shRNA-ctr(ctr), GFP/shRNA- $\alpha$ II spectrin ( $\alpha$ II kd) and GFP/shRNA- $\beta$ III ( $\beta$ III kd). Cells were immunostained with  $\alpha$ II spectrin (magenta) and  $\beta$ III spectrin (white). **(E)** Representative image of PCs transfected with GFP/shRNA- $\alpha$ II spectrin ( $\alpha$ II kd) in sagittal cerebellar tissue at P14. The histogram shows the proportions of dendritic segments located at the indicated distance from a plane fitted to the dendrites. **(F)** Top panels: Morphology of PCs transfected with GFP/shRNA-ctr (ctr), GFP/shRNA- $\alpha$ II spectrin ( $\alpha$ II kd), and GFP/shRNA- $\alpha$ II spectrin together with shRNA-resistant  $\alpha$ II spectrin ( $\alpha$ II kd + rescue). Cells were grown on aligned nanofiber substrates. Bottom panels: Angular distribution of dendritic segments. Scale bars: 20  $\mu$ m.

#### **Figure 4 Analysis of PC dendrite dynamics on aligned nanofiber substrates.**

**(A)** Timelapse images of developing PC dendrites growing on aligned nanofiber substrates from 8 DIV. The orientation of the nanofibers is indicated by a black arrow. Cells are transfected with GFP/shRNA control (ctr, top panels) or GFP/shRNA- $\beta$ III spectrin ( $\beta$ III kd, bottom panels). **(B)** Polar histograms showing the distribution of dendritic terminals growing in the indicated directions in ctr and  $\beta$ III kd cells. Angles between elongated dendrites and fibers were measured.  $n = 10$  cells for ctr and  $\beta$ III kd cells. **(C and D)** Magnified views of timelapse images of dendrites transfected with GFP/shRNA-ctr (C) or GFP/shRNA- $\beta$ III spectrin (D). Blue arrows indicate the growth direction of the dendrites. Branches are formed at the terminals of growing dendrites (C, terminal branching at 28 and 40 hr) or sprout from the lateral side (D, lateral branching at 36 hr). For the analysis, we defined collateral branch formation more than 15  $\mu$ m away from the terminal as lateral branching. Note that the growth orientations are deflected by branch formation (see arrows at 40 hr in the ctr and 36 hr in  $\beta$ III kd). Recovery to the original orientation was observed upon further progression in ctr (C) but not in  $\beta$ III kd cells (D). **(E and F)** Polar histogram showing the deflection angle between parent and sister branches at terminal branching (left) or lateral branching (right) in ctr (E) and  $\beta$ III kd cells (D). **(G and H)** Box graphs showing the proportion of lateral branching (G) and the branching frequency of growing dendrites (H). Statistical significance was evaluated by using the Wilcoxon rank-sum test.  $N = 11$  cells for ctr, 12 cells for  $\beta$ III kd. **(I)** Graphs indicate the growth orientation of dendritic terminals at the time immediately after branch formation (left) and 9 hours after branch formation (right) in ctr (left) or  $\beta$ III kd cells (right).  $n = 48$  dendritic terminals from 5 cells for ctr, 76 dendritic terminals from 5 cells for  $\beta$ III kd cells. Fifteen randomly selected growing terminals are indicated as gray points.

Statistical significance was evaluated by the Wilcoxon signed-rank test. Scale bars: 40  $\mu$ m in (A), 10  $\mu$ m in (C) and (D).

### Figure 5 $\beta$ III spectrin knockdown induces the extension of lateral-oriented branches

(A) Growing dendritic arbors in GFP/shRNA-ctr (ctr)- or GFP/shRNA- $\beta$ III ( $\beta$ III kd)-transfected cells in the vermis region in coronal cerebellar slices at P14. (B) Polar histogram showing the angular distribution of the main dendritic arbor in ctr (upper) and  $\beta$ III kd (lower) cells.  $n = 15$  dendrites for ctr and  $n = 13$  dendrites for  $\beta$ III kd. (C) Quantification of the number of laterally oriented branches sprouted from main dendrites (50  $\mu$ m).  $n = 15$  dendrites for each dataset. (D) Images are magnified views of the insets in (A). (E) Quantification of the length of dendritic protrusions in ctr or  $\beta$ III kd cells. Ctr:  $n = 231$  protrusions from 10 cells.  $\beta$ III kd:  $n = 102$  protrusions from 10 cells. (F) The number of abnormally long ( $> 5 \mu$ m) dendritic protrusions per 50  $\mu$ m of the dendritic segment in ctr or  $\beta$ III kd cells.  $n = 18$  dendrites for ctr,  $n = 15$  dendrites for  $\beta$ III kd. (G) Number of dendritic protrusions per 10  $\mu$ m of the dendritic segment at the distal region in ctr or  $\beta$ III kd cells.  $n = 10$  for ctr and  $\beta$ III kd. Statistical analyses were carried out by using the Wilcoxon rank sum test (C) and Student's t-test (E-G). Scale bars: 5  $\mu$ m in (A) and (D).

### Figure 6 Abnormal extension of dendritic protrusions is induced by the loss of $\beta$ III spectrin

(A and B) Representative images of the growing dendritic terminals of PCs transfected with shRNA-ctr (A, ctr) or shRNA- $\beta$ III spectrin (B,  $\beta$ III kd). Cells were cultured on aligned nanofibers and stained with the postsynaptic protein GluR $\delta$ 2 (GluD2, magenta) after fixation at 10 DIV. (C and D) Quantification of the length of the protrusions (C) and the number of dendritic protrusions per micron (D) in ctr or  $\beta$ III kd PC dendrites. Ctr:  $n = 333$  protrusions from 8 cells for ctr and  $n = 136$  protrusions from 8 cells. Wilcoxon rank-sum tests were carried out to evaluate statistical significance. (E) The orientation of dendritic protrusions with respect to nanofibers. Ctr:  $n = 320$  protrusions from 7 cells.  $\beta$ III kd:  $n = 127$  protrusions from 8 cells. (F) Schematic explanation of growing PC dendrites (green) on aligned GC axons (light orange) in ctr or  $\beta$ III kd cells. PC dendrites express postsynaptic GluD2, which functions as a synaptic glue at their protrusions (magenta). In the ctr PCs, the dendrites grow perpendicular to GC axons, while their protrusions orient parallel to GC axons.  $\beta$ III kd PCs extend abnormally elongated protrusions parallel to parallel fibers. (G) Localization of  $\beta$ III spectrin (cyan) at the distal end of the growing dendrite in a GFP-labeled shRNA-ctr cell grown on a glass substrate. (H) Magnified views of actin signals and  $\beta$ III spectrin at the dendritic filopodia in the ctr cells. HA-actin was transfected to visualize actin signals. (I) Intensity profiles of  $\beta$ III spectrin and HA-actin along the dotted line marking a dendritic protrusion in (H). The black dotted line in the graph indicates the boundary between the protrusion and the shaft. (J) Left: Representative image of the distal end of the growing dendrite of a GFP-labeled  $\beta$ III spectrin kd cell grown on a glass substrate. Right:

Magnified views of actin signals in the dendritic protrusions (Type 1: thin and long, Type 2: short and stubby) of  $\beta$ III kd cells. **(K)** Intensity profiles of HA-actin along the dotted line marking the growing terminal of the dendrites in (J). Scale bars: 5  $\mu$ m in (A), (B), (G) and (J, left), 1  $\mu$ m in (H) and (J, right panels).

**Figure 7 The invasion of EB3 into dendritic protrusions is facilitated by the loss of  $\beta$ III spectrin**

**(A, B)** Timelapse imaging of EB3-EGFP in the dendrites of mCherry/shRNA-ctr (A, ctr) or mCherry/shRNA- $\beta$ III spectrin (B,  $\beta$ III kd) cells. Images are the maximum projections of EB3-EGFP spots during 150 sec of observation. Time-lapse images were recorded in the most distal (left) and the proximal (right) regions every three seconds. The dotted line indicates the contour of the dendrites visualized by the mCherry signals. EB3-EGFP signals in the dendritic protrusions are indicated by arrows. **(C)** The ratio of filopodia targeted by EB3-EGFP within 150 seconds of imaging. Statistical analysis was performed by the Steel-Dwass multiple comparison test. **(D)** Example of filopodial extension triggered by EB3-labeled microtubule polymerization in the proximal dendrite region in  $\beta$ III kd cells. Bottom panels show time-series images of the boxed region in the top image. Figures show progressions every 12 seconds. **(E)** Quantification of the mean speed of EB3 spots traveling within PC dendrites. Statistical significance was evaluated by the Wilcoxon rank sum test. Distal ctr: n = 377 from 19 dendrites, distal  $\beta$ III kd n = 318 from 13 dendrites, proximal ctr: n = 174 from 12 dendrites, proximal  $\beta$ III kd n = 148 from 8 dendrites. **(F)** Schematic hypothesis of  $\beta$ III spectrin function in the regulation of microtubule dynamics.  $\beta$ III spectrin might suppress microtubule invasion into dendritic protrusions. Loss of  $\beta$ III spectrin results in the formation of a lateral branch, probably due to frequent microtubule invasion. Scale bars: 3  $\mu$ m in (A) and (B), 2  $\mu$ m in (D)

**Figure 8 Functional analysis of the effect of SCA5-related mutations in the regulation of dendrite orientation**

**(A)** Domain structure of  $\beta$ III spectrin and familial mutations associated with spinocerebellar ataxia type 5 (SCA5). **(B)** Localization of myc-tagged  $\beta$ III spectrin wild-type (WT), L253P, E532-M544 del, and L629-R643 delinsW mutant proteins in PCs grown on coverslips. Cells were fixed at 9 DIV. **(C)** Quantification of the signal intensity ratio (distal versus proximal) of  $\beta$ III molecules in PC dendrites. N = 10 for WT, n = 14 for L253P, n = 14 for E532-M544 del, and n = 14 for L629-R634 delinsW. Statistical significance was analyzed with the Kruskal-Wallis test followed by the Dunnett test. **(D)** Representative images of PCs transfected with GFP/shRNA- $\beta$ III spectrin plus myc-tagged  $\beta$ III spectrin wild-type (WT), L253P, E532-M544 del, and L629-R643 delinsW mutant proteins. PCs were grown on aligned nanofibers. The dendritic orientations of PCs expressing each  $\beta$ III molecule are shown with polar histograms. n = 13 for WT, n = 14 for L253P, n = 20 for E532-M544 del, and n = 16 for L629-R634 delinsW. Scale bars: 10  $\mu$ m in (B), 20  $\mu$ m in (D).

## Supplementary figure legends

### Figure S1 Validation of shRNA targeting $\beta$ III spectrin in dissociation culture

Representative images of cerebellar Purkinje cells transfected with a plasmid containing EGFP/shRNA control (ctr) or EGFP/shRNA  $\beta$ III spectrin ( $\beta$ III kd). Cells were stained with anti-calbindin (magenta) and anti- $\beta$ III spectrin (white) antibodies. The calbindin-positive Purkinje cells transfected with the  $\beta$ III kd plasmid lacked  $\beta$ III spectrin signals. Scale bars: 20  $\mu$ m.

### Figure S2 Quantitative analysis of the planarity of PC dendrites in cerebellar tissue

(A) Representative image of cerebellar Purkinje cells labeled with GFP in a sagittal cerebellar slice at P14. (B) Skeletonized image of the Purkinje cell dendrites in (A). Magenta points on the skeletonized dendrite were randomly selected. (C) A three-dimensional view of the skeletonized dendrite, randomly selected points, and a plane fitted to the dendrites. (D) A side view of randomly selected points and the dendritic plane.

### Figure S3 Pharmacological inhibition of neuronal activities between GCs-PCs

Morphology of Purkinje cell dendrites grown on aligned nanofiber substrates with or without neuronal activity inhibitors (10  $\mu$ M DNQX: AMPA/kinase receptor antagonist and/or 100  $\mu$ M CPCCOEt: mGluR1 antagonist). Purkinje cells were labeled with calbindin (green). Polar histograms indicate the distribution of dendrite orientations with respect to nanofibers. Scale bar: 20  $\mu$ m.

### Figure S4 CRISPR/Cas9-based $\beta$ III spectrin knockout affects the perpendicular interaction between PC dendrites and GC axons.

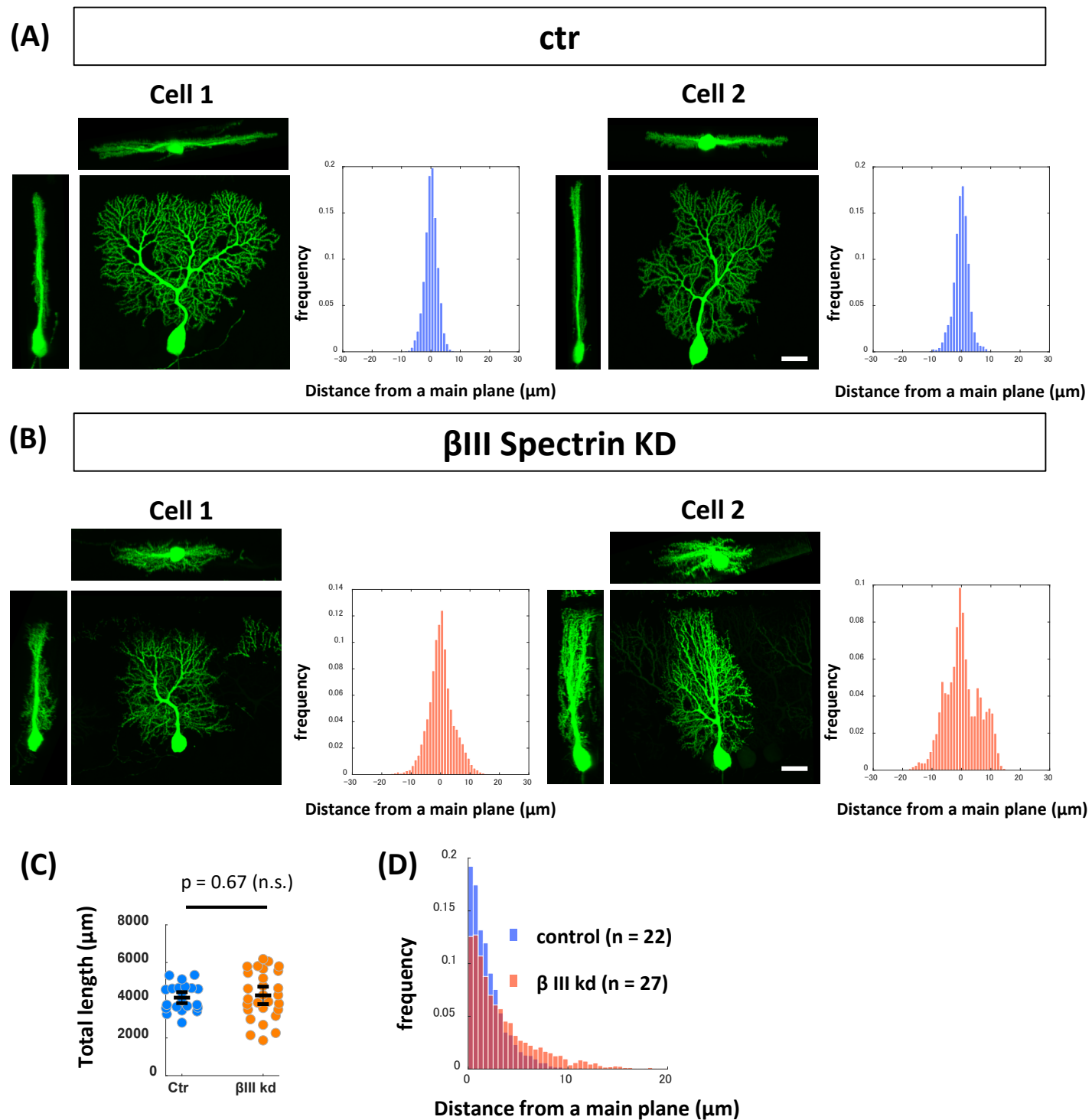
Representative images of Purkinje cells on aligned fibers transfected with CRISPR/Cas9 vectors (left: control empty vector, right:  $\beta$ III spectrin target sequence). Cells were stained with anti- $\beta$ III spectrin (magenta). The  $\beta$ III spectrin knockout cell exhibits a dendrite elongating in an abnormal orientation. Scale bar: 30  $\mu$ m.

### Figure S5 Membrane periodic structure of $\beta$ III spectrin in PC dendrites

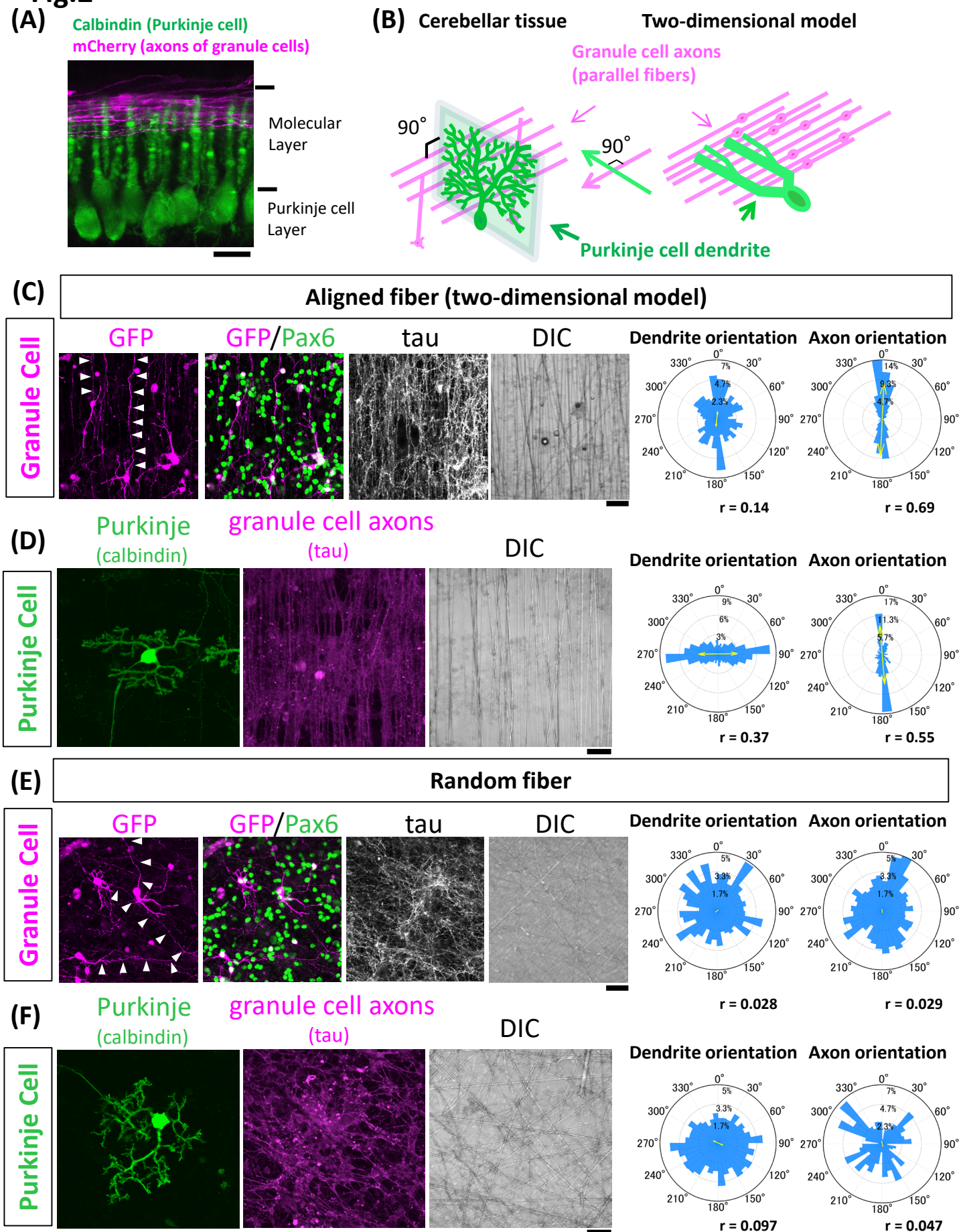
(A and B) Representative STED image of  $\beta$ III spectrin in the proximal region (A) and distal region (B) of developing PC dendrites. (C) ROI1-3 (ROI1: dendritic shaft in (A), ROI2-3: dendritic filopodia in (B)) are magnified views. The normalized intensities of  $\beta$ III spectrin repeats in ROIs 1-3 are shown by line plots below. Gray dotted lines are drawn every 185 nm from the first peak of the  $\beta$ III spectrin signal. (D) The histogram indicates the distribution of the spacing of repeated  $\beta$ III spectrin structures in the dendritic shaft (blue) and the base of dendritic protrusions (red). Shaft: n = 85 from 11 dendrites. Base of protrusions: n = 103 from 13 dendrites (dendritic base). (E) Another example of a STED

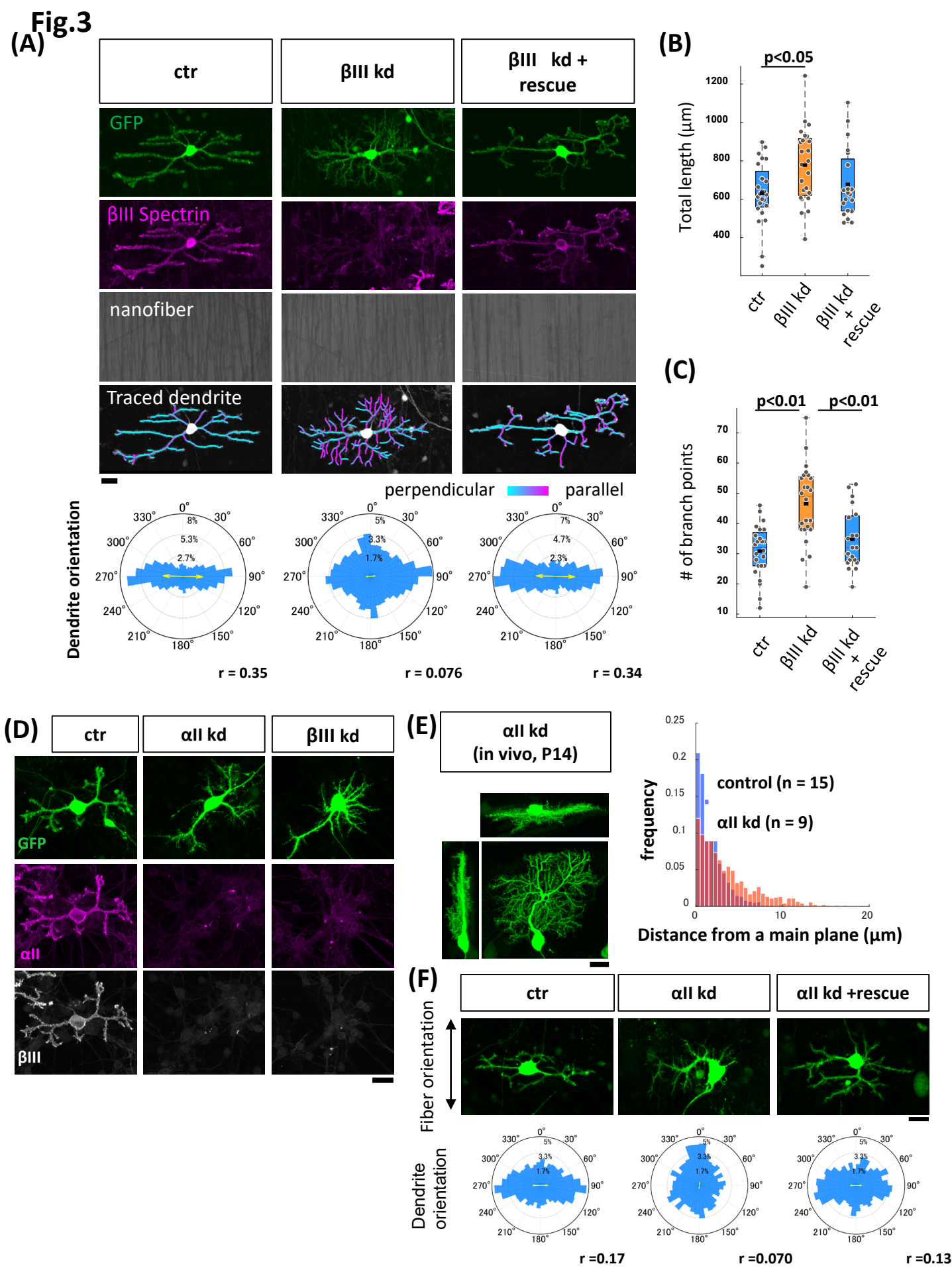
image of  $\beta$ III spectrin in the shaft region of a developing Purkinje cell dendrite. (F) ROI4-6 are magnified views of the boxed regions in (A). Normalized intensities of  $\beta$ III spectrin repeats are shown by line plots below. Scale bars: 2  $\mu$ m in (A), (B) and (E). 200 nm in (C) and (F).

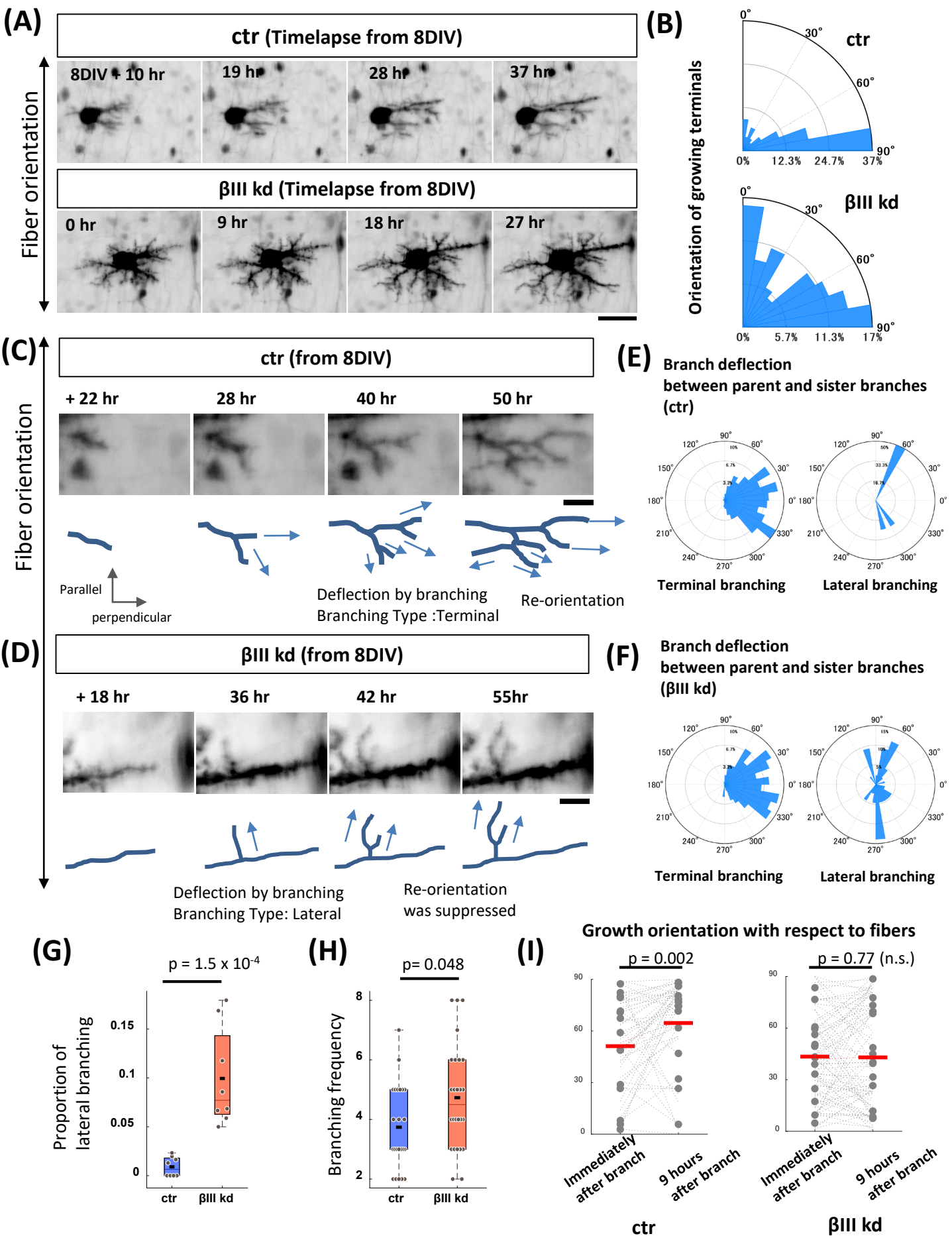
**Fig.1**

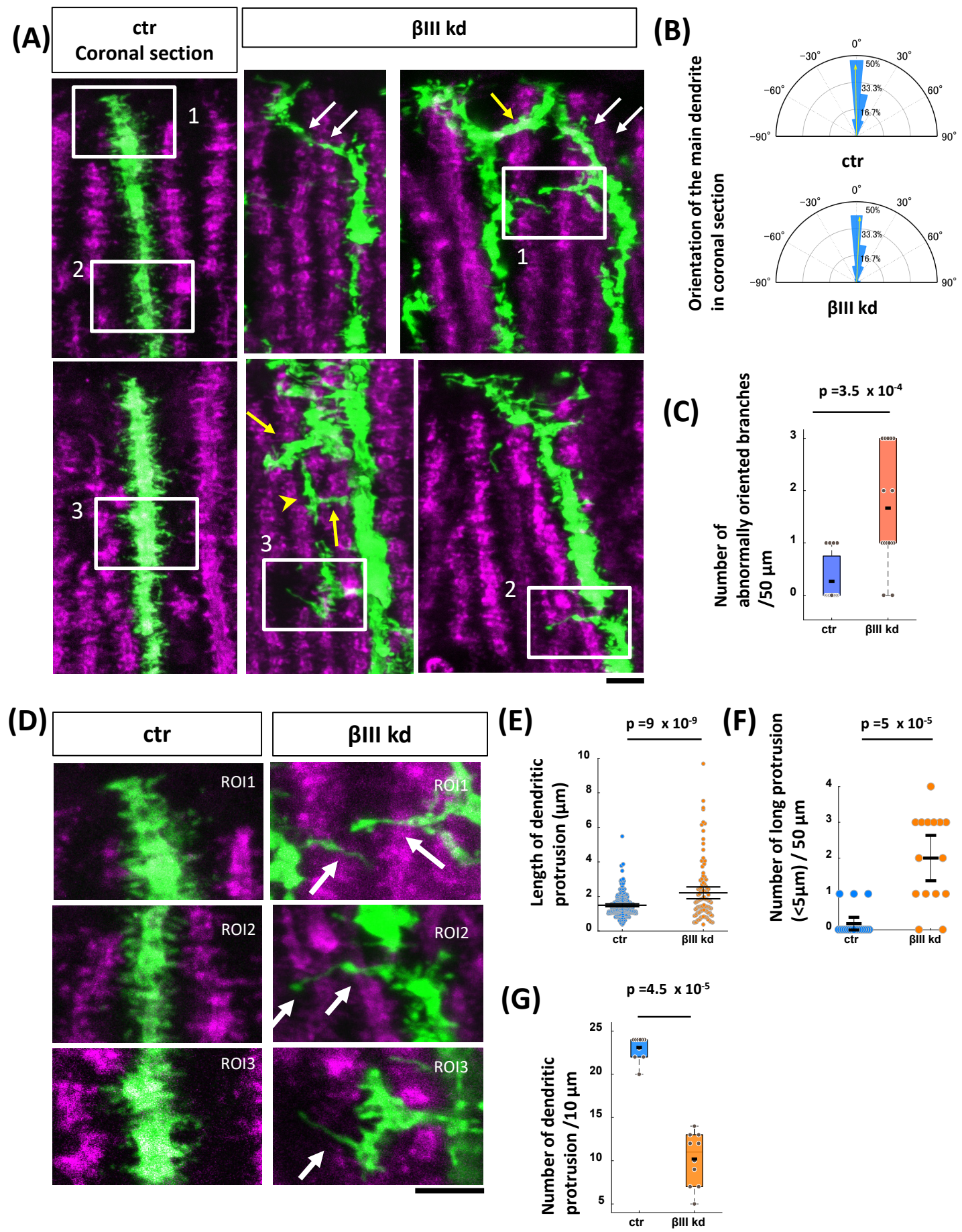


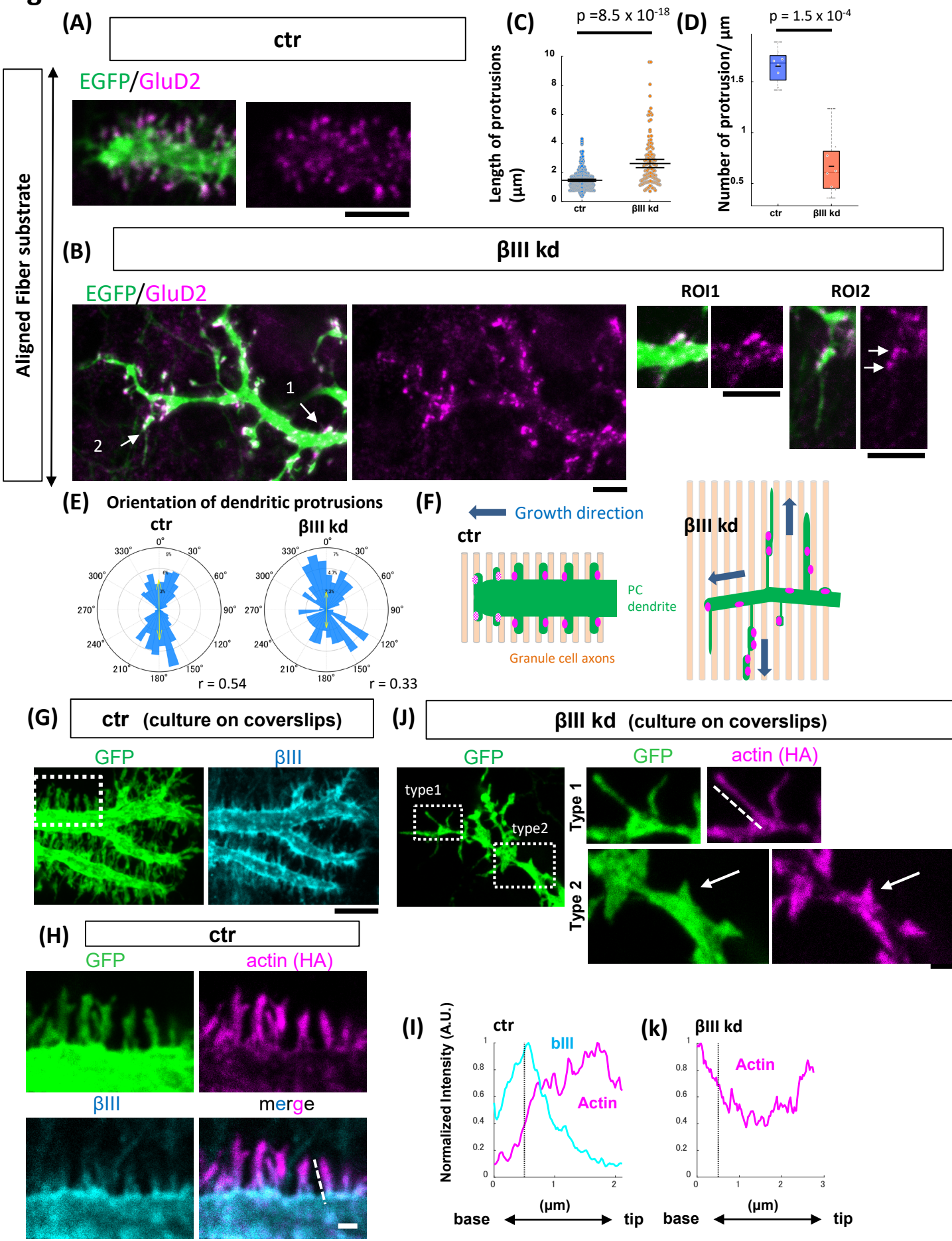
**Fig.2**

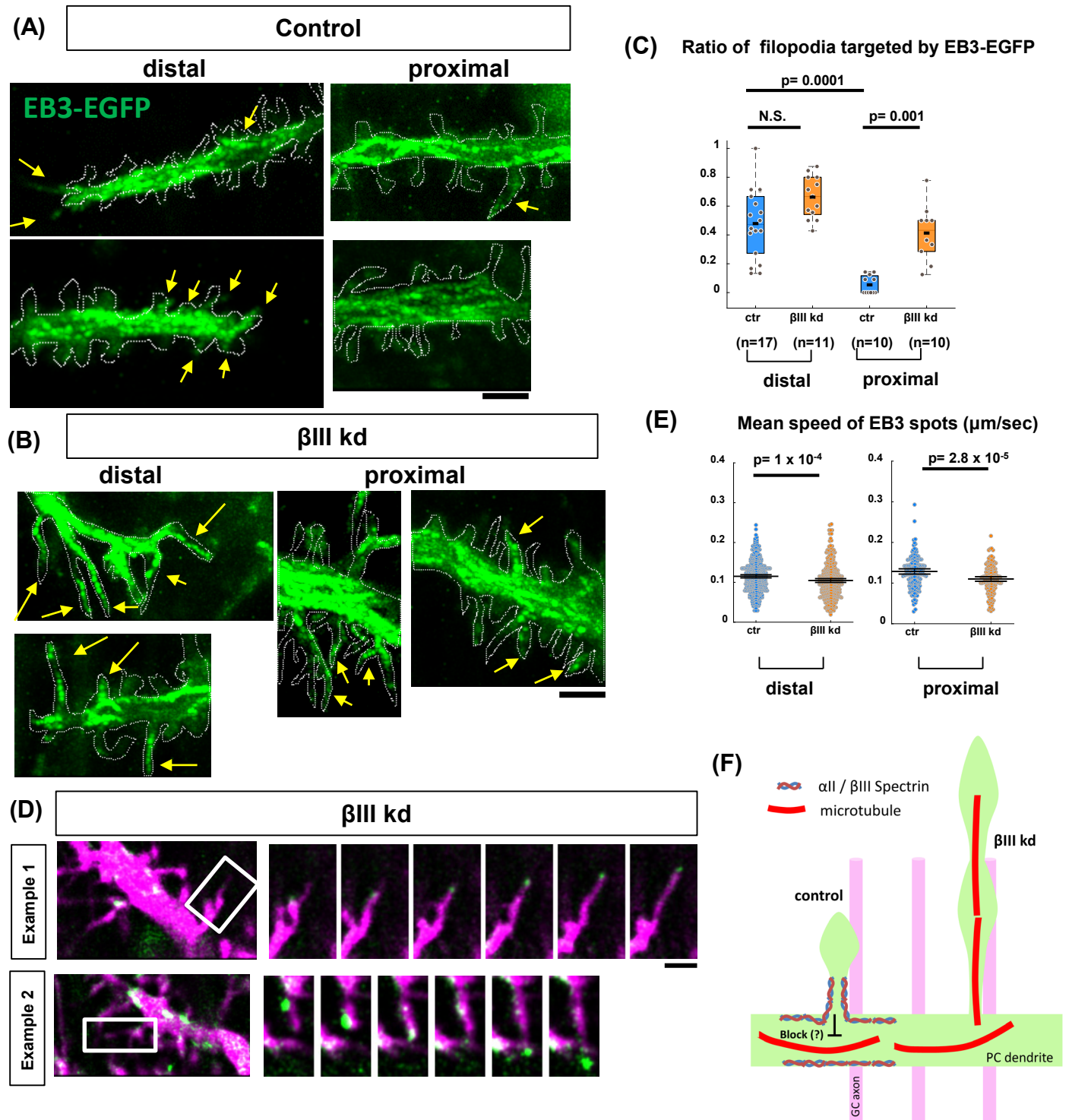




**Fig. 4**

**Fig.5**

**Fig.6**

**Fig.7**

**Fig.8**

